Chapter Ten

Spatial multiplexing: modelling

Filipe Ferreira, Christian Costa, Sygletos Stylianos, Andrew Ellis
Aston Institute of Photonic Technologies University
Aston University
Birmingham, B47ET, United Kingdom
f.ferreira@aston.ac.uk

Spatial-division multiplexing has been proposed as a next-generation solution to overcome the imminent exhaustion of the capacity of current single-mode fiber based systems. However, these systems presented additional challenges such as the overall group-delay spread due to differential spatial-path delay and linear spatial-path coupling, and inter-mode nonlinear effects. The accurate modelling of these effects is preponderant on the performance optimization of mode-division multiplexing systems. This chapter reviews a method for the semi-analytical modelling of linear mode coupling. Simulations using this model matched the analytical predictions for the statistics of group-delays in few-mode fiber links, considering different coupling regimes with and without mode delay management. Furthermore, this chapter reviews the study of nonlinear performance of few-mode fiber links operating in all different linear coupling regimes and mode delay maps. The optimum link configurations minimizing the nonlinear penalty at practical levels of equalization complexity are presented. Finally, the limits of the extension of the Manakov approximation to the multi-mode case are accurately validated against a fully stochastic model developed considering distribution linear mode coupling.

Book Title
First Author & Second Author

www.panstanford.com

10.1 INTRODUCTION

Mode-division multiplexing (MDM) over few-mode fibers (FMFs) is emerging as an attractive solution to overcome the capacity limit of single-mode fibers (SMFs) [1, 2]. However, the multitude of guided modes introduces new impairments that have to be addressed in order to reach FMFs' full capacity, namely: group delay (GD) spread [3-6] given the interplay between differential mode delay (DMD) and linear mode coupling (XT), and inter-mode nonlinear effects [7-10].

To correctly estimate the GD spread and the performance of a MDM equalizer, the mode coupling arising from the waveguide imperfections [3], need to be correctly modelled. Thereby, intense research has been accomplished to study the statistics of GDs analytically [4, 11-14] and numerically [15-19]. A significant number of works assume systems operating in the strong mode coupling regime, e.g. [11, 14], and consider a multi-section model where mode coupling is introduced through random unitary matrices each section, where the length of each section must be longer than the correlation length. However, few-mode fibers ([20-23]) usually operate in the weak or intermediate coupling regime for transmission distances 100-1000km. Even though strong mode coupling can be assumed within groups of degenerate modes [24], the mode coupling between groups of non-degenerate modes cannot either be considered negligible or strong. Note that, nonlinear simulation requires a step-size much smaller than nonlinear effective length (~20 km) [25], thus the generation of coupling matrices with the appropriate level for 10-100m is required. Therefore, models considering random unitary matrices do not cover many of the cases of interest.

To model systems operating in the weak and intermediate coupling regime, the introduction of coupling in the form of misaligned fiber splices in each section of a multi-section model was proposed [16]. In this case, the mode coupling matrices are obtained using an overlap integral approach. However, the matrix elements obtained this way present two limitations. First, even though the coefficients are effective in describing the mode power distribution, they fail to consider phase effects thereby appropriate only for incoherent sources 0. Second, the coupling elements inevitably include mode dependent loss given the nature of the overlap integral. Even though splices do introduce mode dependent loss, splices are here being used as a discrete representation of continuous

imperfections which may introduce or not introduce mode dependent loss. Therefore, a model able to separate mode coupling from mode dependent loss is preferable. Recently, the authors have presented a semi-analytical model capable of describing the linear mode coupling for fibers operating in the intermediate coupling regime [17, 18]. Such method was demonstrated to match the analytical predictions for group-delay in few-mode fiber links [26, 27].

In the nonlinear regime, it has been shown that MDM systems performance can be dominated by inter-mode interactions for low DMD and low XT [28], and that high XT significantly reduces intermodal nonlinear [29]. However, in the intermediate coupling regime, the nature of the dependence of the nonlinear distortion on the (distributed) XT strength and DMD has only recently started being studied [10, 30] for mode delay uncompensated and compensated links. Recently, the authors have modified the single-mode split-step Fourier method to include semi-analytical solutions for linear mode coupling of arbitrary strength. Using such model, the authors were able to accurately study for the first time the nonlinear distortion in FMFs operating in the intermediate coupling regime [10, 30].

This chapter presents the derivation of a semi-analytical solution method for the linear mode coupling equations, and validate the group-delay spreading predictions for different coupling regimes and different link configurations. A validation of a multi-section model using semi-analytical solutions is presented for non-GD managed links by matching different analytical predictions for the statistics of the GDs, namely: standard deviation, probability density function, and cumulative distribution function. Furthermore, a validation of the multi-section model for GD managed links is presented by matching the analytical predictions for standard deviation of the GDs. Finally, this chapter reviews the proposed few-mode split-step Fourier method. The nonlinear performance of FMFs is studied for all different linear coupling regimes and mode delay maps, in order to find the optimum link configuration minimizing the nonlinear penalty for practical equalization complexities. Moreover, the regimes under which the extension of the single-mode Manakov approximation to the multi-mode case [8, 29] is valid are assessed, considering the transmission of wavelength multiplexed channels in each of the polarization modes over the fully stochastic model presented including distributed XT.

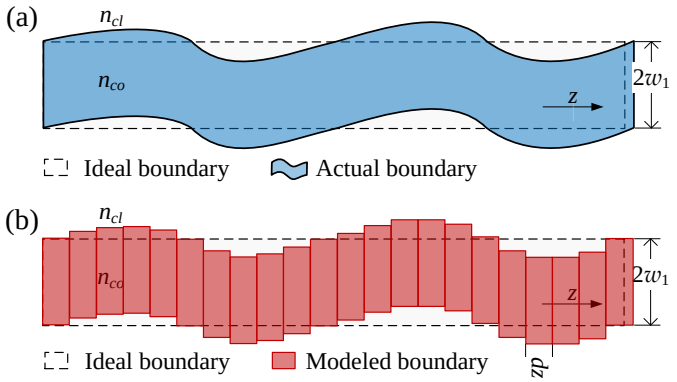

Figure 1. Fiber dielectric waveguide with distorted core-cladding boundary.

10.2 COUPLED-MODE THEORY FOR FEW-MODE FIBERS

The linear mode coupling in few-mode fibers is due to refractive-index inhomogeneities or small deviations of the core-cladding boundary caused by perturbations introduced during the fabrication process or by mechanical stresses imposed on the fiber in the field. Fig. 1 (a) shows a fiber dielectric waveguide with distorted core-cladding boundary. These imperfections cause the modes of the fiber to couple among each other. When exciting a pure mode at the fiber beginning, some of its power is transferred to other guided modes. This power transfer results in signal distortion because each guided mode travels at its own characteristic group velocity. Therefore, the equalization of the received signal must span over a time window that covers all the significant distortions undergone by a given information symbol.

Mode coupling may even be a desirable effect. The mode delay spread can be reduced by introducing a significant amount of distributed coupling among all guided modes which introduces a sufficiently strong averaging effect of the different mode group velocities, see Section 10.5. However, in mode delay compensated fiber links, mode coupling may or may not be desirable, as discussed in Section 10.4.

10.2.1 *Coupled-Mode Equations*

The perturbations that couple the ideal modes of the ideal waveguide can be described by variations of the dielectric tensor. This is, the perturbed dielectric tensor (ε_p) as a function of the space coordinates is written as:

$$\varepsilon_p(x,y,z) = \varepsilon_u(x,y) + \Delta\varepsilon(x,y,z) \tag{1}$$

where $\varepsilon_u(x,y)$ is the unperturbed part of the dielectric tensor, thereby invariant with the fiber longitudinal coordinate z, and $\Delta\varepsilon(x,y,z)$ represents the dielectric perturbation, which in the general case varies with all space coordinates. Eq. (1) can adequately describe the core-cladding perturbations in Fig. 1 (a).

If an arbitrary field of frequency ω is excited at $z = 0$, the propagation of this field in the unperturbed dielectric waveguide can be expressed as a linear combination of the ideal modes:

$$\mathbf{E}(x,y,z,t) = \sum A_m(z,t)\mathbf{E}_m(x,y)e^{j(\omega t-\beta_m z)} \tag{2}$$

where m is the mode index, $A_m(z,t)$ is the slowly varying mode field envelope, β_{0m} is the mode propagation constant at ω, and $\mathbf{E}_m(x,y)$ is the electric field distribution.

In the presence of a dielectric perturbation $\Delta\varepsilon(x,y,z)$, the coupling between the ideal modes are described by the following coupled-mode equations [3, 4, 31]:

$$\left[\partial_z + \beta_{1m}\partial_t - j\frac{\beta_{2m}}{2}\partial_t^2 + j\frac{\beta_{3m}}{6}\partial_t^3 \ldots\right] A_m(z,t) = -j\sum_n C_{m,n}(z)\,A_n(z,t)\,e^{j(\beta_{0m}-\beta_{0n})z} \tag{3}$$

$$C_{m,n}(z) = \frac{\omega\varepsilon_0}{4}\int\int_{-\infty}^{+\infty}\left[\Delta\varepsilon(x,y,z)\right]\mathbf{E}_m^*\cdot\mathbf{E}_n dxdy \tag{4}$$

where β_{lm} is the l^{th} order coefficient of a Taylor series expansion of $\beta_m(\omega)$ centered at the carrier frequency ω. $C_{m,n}$ are the coupling coefficients given by the area integral of the dot product of the electrical fields of mode m and mode n, over the area where the permittivity perturbation $\Delta\varepsilon(x,y,z) \neq 0$.

For the general case, where $\Delta\varepsilon$ is varying continuously with z, so is $C_{m,n}$, the solution of the coupling operator in (1) can only be achieved using numerical methods, e.g. Runge-Kutta method. However, the usage of these methods is computationally inviable for simulation of long-haul

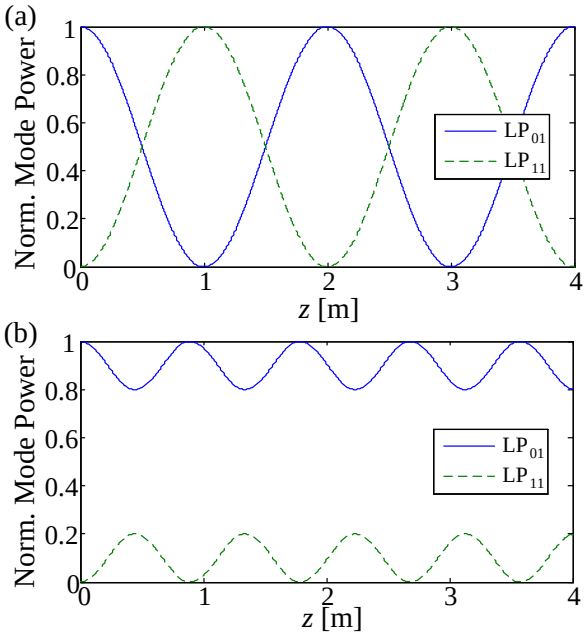

Figure 2. Fiber dielectric waveguide with distorted core-cladding boundary.

transmission links. To overcome such limitation, we propose a model that discretizes the core-cladding fluctuations by dividing the fiber in multiple sections, each with a random displacement of the core center position constant along the section. In this case, the dielectric tensor is given by:

$$\varepsilon_p(x,y,z) = \varepsilon_{r0}(x+\delta x(z),y+\delta y(z),z) \tag{5}$$

where δx and δy are the random displacement of the abscissa and ordinate coordinates, respectively. Fig. 1 (b) shows a diagram of the discretization of the core-cladding fluctuations given the proposed method. In this case, each section has constant coupling coefficients. Therefore, in theory it should be possible to find (semi-)analytical solutions for the coupling operator present in (3).

Assuming the fiber section length is much shorter than both the dispersion length $L_D = T_0^2/|\beta_{2m}|$ and the walk-off length $L_W = T_0/|\beta_{1m}-\beta_{1n}|$, where T_0 is a measure of the pulse width, an approximate solution of (3) can be obtained by assuming the dispersive effects and linear coupling effects act independently. In the following, we will focus on

finding a (semi-)analytical solution for the coupling operator, this is, we will be trying to solve:

$$\partial_z A_m(z,t) = -\mathrm{j}\sum_n C_{m,n}(z) A_n(z,t) e^{\mathrm{j}(\beta_{0m}-\beta_{0n})z} \tag{6}$$

10.2.2 *Coupled-Mode Equations Solution for Two-Mode Fibers*

The simple case of a two-mode fiber, where only the coupling between the LP_{01} mode ($m = 1$) and the LP_{11} mode ($n = 2$) is present, (6) can be solved analytically in each section [3]:

$$A_1(z) = e^{\mathrm{j}(\Delta\beta/2)z}\left[\cos sz - \mathrm{j}\frac{\Delta\beta}{2}\frac{\sin sz}{s} \quad -\mathrm{j}\kappa\frac{\sin sz}{s}\right]\begin{bmatrix}A_1(0)\\A_2(0)\end{bmatrix} \tag{7}$$

$$A_2(z) = e^{-\mathrm{j}(\Delta\beta/2)z}\left[-\mathrm{j}\kappa^*\frac{\sin sz}{s} \quad \cos sz + \mathrm{j}\frac{\Delta\beta}{2}\frac{\sin sz}{s}\right]\begin{bmatrix}A_1(0)\\A_2(0)\end{bmatrix} \tag{8}$$

where $\Delta\beta = \beta_{01} - \beta_{02}$, $s^2 = \kappa\kappa^* + (\Delta\beta/2)^2$, and $\kappa = C_{12} = C_{21}^*$. From (7) and (8), it can be concluded that the coupling strength depends on the relation between $|\kappa|^2$ and $\Delta\beta^2$.

Fig. 2 a) and Fig. 2 b) show the mode powers $|A_1|^2$ and $|A_2|^2$ as functions of the interaction distance z, for $\Delta\beta = 0$ and for $\Delta\beta = 4|\kappa|$, respectively, with $\kappa = \pi/2$. Fig. 2 shows that the coupling efficiency is 100 % when the phase mismatch is zero, a full power swap happens for every $|\kappa|z$ odd multiple of $\pi/2$. However, if the phase mismatch is different from zero the coupling is no longer the power coupling is incomplete, for $\Delta\beta = 2|\kappa|$ the maximum coupling is ½.

For higher number of modes, the dependence of the coupling strength on the phase mismatch and on the coupling coefficient should follow similar dependencies. Next section presents a solution method for higher number of modes.

10.3 SEMI-ANALYTICAL SOLUTIONS FOR HIGHER-ORDER MODES

For the simple case of a fiber with two modes, (6) can be easily solved by hand, however, this method becomes endless for higher number of

modes. The use of a numerical method for the solution of (6), such as the Runge-Kutta-Fehlberg (RK45) method, is also not an option since it would be necessary to solve these equations for each fiber section with different fiber displacements, thus leading to computation times that are unaffordable in most applications. Therefore, an analytical approach is desirable.

Our approach starts by taking the Fourier Transform of (6) on z to avoid the complex exponentials, obtaining:

$$A_m(w_z) = -\frac{\mathrm{j}}{w_z}\sum_n C_{m,n}A_n(w_z - \Delta\beta_{m,n}) \tag{9}$$

where w_z is the spatial frequency and $\Delta\beta_{m,n} = \beta_{0m}-\beta_{0n}$. The system of equations (9) can be solved by substitution, thereby eliminating each A_p from all the equations for all $p \neq m$, obtaining an equation for A_m which can be written as:

$$A_m(w_z)\cdot\left[a_{m,R}(\mathrm{j}w_z)^R + \ldots + a_{m,0}(\mathrm{j}w_z)^0\right] = 0 \tag{10}$$

where R is equal to $2(M - 1)$, with M equal to the number of modes, and $a_{m,r}$ are functions of $\Delta\beta_{mn}$ and C_{mn}. The process described must be performed for $m = 1, \ldots, M$ to obtain equations like (10) for each mode. Now, by applying the inverse Fourier transform to (10), a differential equation with constant coefficients is obtained which can be solved using the method of the characteristic polynomial, obtaining:

$$A_m(z) = b_{m,1}e^{s_{m,1}z} + \ldots + b_{m,R}e^{s_{m,R}z} \tag{11}$$

where $s_{m,r}$ are the characteristic polynomial roots and $b_{m,r}$ are constants that can be determined from the initial conditions at $z = 0$ obtained by differentiating (6), $(d_z{}^iA_m)_{z=0}$, and equating the results. Finally, the coefficients $b_{m,r}$ are the solutions of the linear equations system:

$$\begin{bmatrix} s_{m,1} & \cdots & s_{m,N} \\ \vdots & \ddots & \vdots \\ s_{m,1}^{2(M-1)} & \cdots & s_{m,N}^{2(M-1)} \end{bmatrix}\begin{bmatrix} b_{m,1} \\ \vdots \\ b_{m,R} \end{bmatrix} = \begin{bmatrix} \left(d_z^0 A_m\right)_{z=0} \\ \vdots \\ \left(d_m^{2(M-1)}A_m\right)_{z=0} \end{bmatrix} \tag{12}$$

The solution method described is easily applied using a software tool with symbolic computation capability. We have used the Symbolic Math

Toolbox from Matlab® to generate equations for $a_{m,r}$ and $(d_z{}^i A_m)_{z=0}$ as function of $\Delta\beta_{mn}$ and C_{mn}. Finally, the derived equations can be written into a conventional text file and compiled using any programming language (we used a C-compiler). Afterwards, those equations can be evaluated allowing to find the roots of the polynomials in (10) and to solve the system of linear equations in (12).
In summary, instead of numerically solving a coupled-system of M differential equations (6), the method proposed requires the finding the roots of a $2(M-1)$ order polynomial, for which efficient and accurate algorithms are available, e.g. Bairstow's method [32], and the solution of a system of linear equations (12).

10.3.1 *Analytical expressions for the three-modes case*

The analytical expression for $a_{m,r}$ and $(d_z{}^r A_m)_{z=0}$ as a function of $\Delta\beta_{m,n}$ and $C_{m,n}$ for $M = 3$ are given by equations (13) to (18), obtained executing the MATLAB code presented in 0. Replacing the $\Delta\beta_{m,n}$ and $C_{m,n}$ numeric values in the $a_{m,r}$ analytical equations, the $s_{m,r}$ values can be calculated using algorithms for the calculation of polynomial roots. Moreover, $(d_z{}^r A_m)_{z=0}$ values are obtained replacing the $\Delta\beta_{m,n}$ and $C_{m,n}$ numeric values in the analytical formulas. Finally, the system of linear equations (12) can be numerically solved.

10.3.2 *Analytical expressions for more than three-modes*

The analytical expression for $a_{m,r}$ and $(d_z{}^r A_m)_{z=0}$ as a function of $\Delta\beta_{m,n}$ and $C_{m,n}$ for $M > 3$ can be obtained executing Matlab code similar to that made available in [6]. However, the equations become too long to be printed here in full. See Section 10.13, for the analytical equations for 6-modes and the derivation MATLAB scripts.

$$\begin{bmatrix} a_{1,0} \\ a_{1,1} \\ a_{1,2} \\ a_{1,3} \\ a_{1,4} \end{bmatrix} = \begin{bmatrix} 1 \\ -2\,\mathrm{j}\Delta\beta_{12} - \mathrm{j}\,\Delta\beta_{13} \\ C_{12}{}^2 - \Delta\beta_{12}{}^2 - 2\Delta\beta_{12}\Delta\beta_{13} + C_{13}{}^2 + C_{23}{}^2 \\ \mathrm{j}\left(\Delta\beta_{12}{}^2\Delta\beta_{13} - \Delta\beta_{12}C_{12}{}^2 - 2\,\Delta\beta_{12}C_{13}{}^2 - \Delta\beta_{13}C_{12}{}^2 - \Delta\beta_{12}C_{23}{}^2 - 2\,C_{12}C_{13}C_{23}\right) \\ -\Delta\beta_{12}(\Delta\beta_{12}C_{13}{}^2 + \Delta\beta_{13}C_{12}{}^2 + 2C_{12}C_{13}C_{23}) \end{bmatrix} \tag{13}$$

$$\begin{bmatrix} a_{2,0} \\ a_{2,1} \\ a_{2,2} \\ a_{2,3} \\ a_{2,4} \end{bmatrix} = \begin{bmatrix} -1 \\ -3\mathrm{j}\Delta\beta_{12} + \mathrm{j}\Delta\beta_{13} \\ 3\Delta\beta_{12}^{\,2} - 2\Delta\beta_{12}\Delta\beta_{13} - C_{12}^{\,2} - C_{13}^{\,2} - C_{23}^{\,2} \\ \mathrm{j}\begin{pmatrix} -\Delta\beta_{12}^{\,2}\Delta\beta_{13} - 2\Delta\beta_{12}C_{12}^{\,2} - \Delta\beta_{12}C_{13}^{\,2} + \Delta\beta_{13}C_{12}^{\,2} \\ -2\Delta\beta_{12}C_{23}^{\,2} + \Delta\beta_{12}^{\,3} + 2C_{12}C_{13}C_{23} \end{pmatrix} \\ \Delta\beta_{12}(\Delta\beta_{12}C_{12}^{\,2} - \Delta\beta_{13}C_{12}^{\,2} + \Delta\beta_{12}C_{23}^{\,2} - 2C_{12}C_{13}C_{23}) \end{bmatrix} \tag{14}$$

$$\begin{bmatrix} a_{3,0} \\ a_{3,1} \\ a_{3,2} \\ a_{3,3} \\ a_{3,4} \end{bmatrix} = \begin{bmatrix} -1 \\ \mathrm{j}\Delta\beta_{12} - 3\mathrm{j}\Delta\beta_{13} \\ 3\Delta\beta_{13}^{\,2} - 2\Delta\beta_{12}\Delta\beta_{13} - C_{12}^{\,2} - C_{13}^{\,2} - k_{23}^{\,2} \\ \mathrm{j}\begin{pmatrix} -\Delta\beta_{12}\Delta\beta_{13}^{\,2} + \Delta\beta_{12}k_{13}^{\,2} - \Delta\beta_{13}C_{12}^{\,2} \\ -2\Delta\beta_{13}C_{13}^{\,2} - 2\Delta\beta_{13}C_{23}^{\,2} + \Delta\beta_{13}^{\,3} + 2C_{12}C_{13}C_{23} \end{pmatrix} \\ -\Delta\beta_{13}\left(C_{13}^{\,2}\left(\Delta\beta_{12} - \Delta\beta_{13}\right) - 2\Delta\beta_{13}C_{23} + 2C_{12}C_{13}C_{23}\right) \end{bmatrix} \tag{15}$$

$$\begin{bmatrix} d_z^0 A_1 \\ d_z^1 A_1 \\ d_z^2 A_1 \\ d_z^3 A_1 \end{bmatrix}_{z=0} = \begin{bmatrix} A_1 \\ -\mathrm{j}C_{12}A_2 - \mathrm{j}\,C_{13}A_3 \\ \begin{Bmatrix} -C_{12}(C_{12}A_1 + C_{23}A_3) - C_{13}(C_{13}A_1 + C_{23}A_2) \\ +dB_{12}C_{12}A_2 + dB_{13}C_{13}A_3 \end{Bmatrix} \\ \mathrm{j}\begin{Bmatrix} -C_{12}\begin{pmatrix} -C_{12}(C_{12}A_2 + C_{13}A_3) \\ -C_{23}(C_{13}A_1 + C_{23}A_2) \\ -dB_{12}C_{12}A_1 + dB_{23}C_{23}A_3 \end{pmatrix} \\ -C_{13}\begin{pmatrix} -C_{13}(C_{12}A_2 + C_{13}A_3) \\ -C_{23}(C_{12}A_1 + C_{23}A_3) \\ -dB_{13}C_{13}A_1 - dB_{23}C_{23}A_2 \end{pmatrix} \\ -2dB_{12}C_{12}(C_{12}A_1 + C_{23}A_3) \\ -2dB_{13}C_{13}(C_{13}A_1 + C_{23}A_2) \\ +dB_{12}^{\,2}C_{12}A_2 + dB_{13}^{\,2}C_{13}A_3 \end{Bmatrix} \end{bmatrix} \tag{16}$$

$$\begin{bmatrix} d_z^0 A_2 \\ d_z^1 A_2 \\ d_z^2 A_2 \\ d_z^3 A_2 \end{bmatrix}_{z=0} = \begin{bmatrix} A_2 \\ -\mathrm{j}C_{12}A_1 - \mathrm{j}C_{23}A_3 \\ \left\{ \begin{matrix} -C_{12}(C_{12}A_2 + C_{13}A_3) - C_{23}(C_{13}A_1 + C_{23}A_2) \\ -\Delta\beta_{12}C_{12}A_1 + \Delta\beta_{23}C_{23}A_3 \end{matrix} \right\} \\ \left\{ \begin{matrix} -C_{12}\begin{pmatrix} -C_{12}(C_{12}A_1 + C_{23}A_3) \\ -C_{13}(C_{13}A_1 + C_{23}A_2) \\ +\Delta\beta_{12}C_{12}A_2 + \Delta\beta_{13}C_{13}A_3 \end{pmatrix} \\ \mathrm{j}\left\{ -C_{23}\begin{pmatrix} -C_{13}(C_{12}A_2 + C_{13}A_3) \\ -C_{23}(C_{12}A_1 + C_{23}A_3) \\ -\Delta\beta_{13}C_{13}A_1 - \Delta\beta_{23}C_{23}A_2 \end{pmatrix} \right\} \\ +\ 2\Delta\beta_{12}C_{12}(C_{12}A_2 + C_{13}A_3) \\ -2\Delta\beta_{23}C_{23}(C_{13}A_1 + C_{23}A_2) \\ +\ \Delta\beta_{12}{}^2C_{12}A_1 + \mathrm{j}\Delta\beta_{23}{}^2C_{23}A_3 \end{matrix} \right\} \end{bmatrix} \tag{17}$$

$$\begin{bmatrix} d_z^0 A_3 \\ d_z^1 A_3 \\ d_z^2 A_3 \\ d_z^3 A_3 \end{bmatrix}_{z=0} = \begin{bmatrix} A_3 \\ -\mathrm{j}C_{13}A_1 - \mathrm{j}C_{23}A_2 \\ \left\{ \begin{matrix} -C_{13}(C_{12}A_2 + C_{13}A_3) - C_{23}(C_{12}A_1 + C_{23}A_3) \\ -\Delta\beta_{13}C_{13}A_1 - \Delta\beta_{23}C_{23}A_2 \end{matrix} \right\} \\ \left\{ \begin{matrix} -C_{13}\begin{pmatrix} -C_{12}(C_{12}A_1 + C_{23}A_3) \\ -C_{13}(C_{13}A_1 + C_{23}A_2) \\ +\Delta\beta_{12}C_{12}A_2 + \Delta\beta_{13}C_{13}A_3 \end{pmatrix} \\ \mathrm{j}\left\{ -C_{23}\begin{pmatrix} -C_{12}(C_{12}A_2 + C_{13}A_3) \\ -C_{23}(C_{13}A_1 + C_{23}A_2) \\ -\Delta\beta_{12}C_{12}A_1 + \Delta\beta_{23}C_{23}A_3 \end{pmatrix} \right\} \\ +2\Delta\beta_{13}C_{13}(C_{12}A_2 + C_{13}A_3) \\ +2\Delta\beta_{23}C_{23}(C_{12}A_1 + C_{23}A_3) \\ +\Delta\beta_{13}{}^2C_{13}A_1 + \mathrm{j}\Delta\beta_{23}{}^2C_{23}A_2 \end{matrix} \right\} \end{bmatrix} \tag{18}$$

10.3.3 *Algorithm Complexity*

The RK45 method requires a step-size of a fraction of the beat-length between the two mode-groups most furthest apart, which can easily be of the order of a millimeter or less [24]. In this way, to resolve a one millimeter beat-length, more than 10^4 and 10^6 steps are required for a transmission length of 1 and 100 meters, respectively. Each RK45 step requires six evaluations of a system of M equations (6), each equation with $2(M - 1)$ multiplications, thus totalizing $12M(M - 1)$ multiplication operations per step.

The semi-analytical method proposed uses the Bairstow's method to find the roots of M polynomials of order $2(M - 1)$. This method consists on the progressive division of the original polynomial by quadratic polynomials while adjusting the coefficients of the later. Thus, the method requires $(M - 1)$ polynomial divisions of progressively lower complexity. Assuming the number of multiplications required to be the product of the number of terms of the polynomials involved, the i^{th}-division requires $[(2(M - 1) + 1) - 2(i - 1)](2+1)$, adding up to $3(M^2 - 1)$ multiplication operations. Finally, this figure must be multiplied by the number of iterations for coefficients adjustment, which we cap to be lower than 100, and observed that in general only 20 repetitions were required. Thus, the total complexity is on the order of $60M(M^2 - 1)$.
Finally, the proposed semi-analytical method reduces the number of multiplications required by a factor from 280 to 28000 when transmitting over 1 to 100 meters, for $M = 6$. These factors agree with the observed simulation times.

10.4 SINGLE-SECTION MODELLING

In this section, the semi-analytical solutions of Section 10.3 are validated using the Runge-Kutta-Fehlberg (RK45) method [33]. The fiber considered for guides six linearly polarized (LP) modes: LP_{01}, LP_{11a}, LP_{11b}, LP_{21a}, LP_{21b}, and LP_{02}. It has a relative index gradient at the core–cladding interface 4.5×10^{-3} and a core radius (w_1) of 12.83 μm, optimization details [34]. Table 1 shows the fiber characteristics at 1550nm (for the sake of clarity, the modes were numbered from one to six). Fig. 3 depicts the amplitude of $C_{m,n}$ as a function of the fiber displacement vector for a radial displacement from 0 to $0.3{\cdot}w_1$. Note that, the coupling coefficients were found to be real and symmetric has concluded in [31], therefore only $C_{m,n}$ with $n > m$ are shown. From Fig. 3, the pairs of modes with higher coupling strength can be identified, and it can be verified that the coupling between symmetric modes (LP_{01}, for example) and anti-symmetric modes (LP_{11}, for example) requires a non-symmetrical perturbation. The surfaces shown in Fig. 3 allow the rapid calculation of the coupling coefficients $C_{m,n}$ using interpolation for a random displacement, as required for integration in a modified split-step Fourier method (SSMF).

Table 1. Fiber Properties at 1550 nm.

		u=LP$_{01}$	u=LP$_{02}$	u=LP$_{11a}$	u=LP$_{11b}$	u=LP$_{21a}$	u=LP$_{21b}$
$\Delta\beta_{1,n}/\kappa$ (x10^{-3})		0	7.4	3.7	3.7	7.4	7.4
$\beta^{(1)}_{1,n}$ (ps/km)		0	-2.6	-0.4	-0.4	2.6	2.6
D_n (ps/km/nm)		22.2	21.5	22.2	22.2	21.8	21.8
S_n (ps/km/nm^2)		66.4	61.5	66.2	66.2	63.7	63.7
γ_{uv} (W^{-1}/km)	v=LP01	0.72	0.36	0.36	0.36	0.18	0.18
	v=LP02	0.36	0.36	0.18	0.18	0.18	0.18
	v=LP11a	0.36	0.18	0.55	0.55	0.27	0.27
	v=LP11b	0.36	0.18	0.55	0.55	0.27	0.27
	v=LP21a	0.18	0.18	0.27	0.27	0.41	0.41
	v=LP21b	0.18	0.18	0.27	0.27	0.41	0.41

where κ is the wave number.

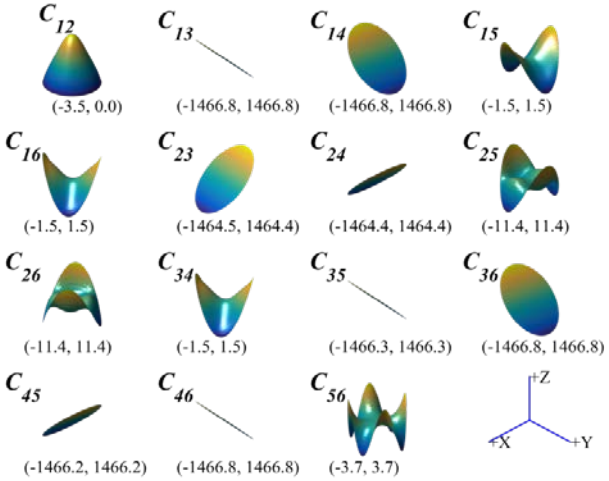

Figure 3. $C_{m,n}$ as a function of the fiber displacement vector, minimum and maximum values as (min, max). Modes numbered as: 1→LP01, 2→LP02, 3→LP11a, 4→LP11b, 5→LP21a, 6→LP21b.

In the following, the semi-analytical (SA) solutions are compared to the numerical solutions obtained using the RK45 method. The variable-step width of the RK45 method is specified considering a relative error tolerance of 10^{-6} and an absolute error tolerance of 10^{-9}. Fig. 4 shows the overlap of the modal powers given by the SA solutions and the modal powers given by the numerical method as a function of z, considering a fiber core displacement of $\rho_d = 0.08 \cdot w_1$ and $\varphi_d = \pi/3$, for an even power distribution between the modes at the input. A very good agreement between the SA and numerical solutions can be noticed in Fig. 4 inset

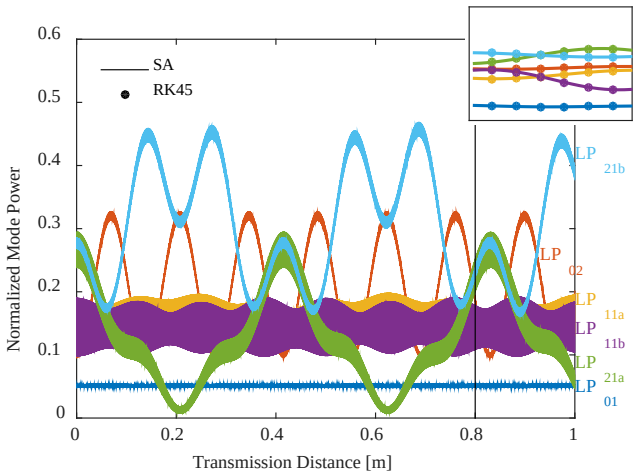

Figure 4. Normalized mode power as a function of the fiber length, for uneven power distribution at the fiber input. The subscripts SA and RK45 were used for semi-analytical and numerical solutions, respectively. The inset shows the excellent agreement between SA and RK45 around 0.8 m.

which zooms in the mode power evolution around 0.8 m. Similar agreement is obtained for different input conditions.

$$MSE_m = \frac{1}{N}\sum_{n=1}^{N}\left|A_m^{SA}(z_n) - A_m^{NUM}(z_n)\right|^2 \tag{19}$$

where $A^{SA}{}_m$ is the SA mode amplitude solution, $A^{NUM}{}_m$ is the numerical mode amplitude solution, and z_n are the discrete points considered in a specific fiber length. MSE_m has been calculated considering 10^5 discrete points equally spaced along a fiber with 1 m, considering ρ_d varying 0 and $0.08 \cdot w_1$ (1000 points equally spaced), and φ_d varying from $-\pi$ to π (1000 points equally spaced). In all the cases tested the MSE_m was always of the order of magnitude of the RK45 absolute tolerance, as verified by repeating the error calculation for different tolerance values. Therefore, it can be concluded that the semi-analytical method proposed provides an accurate estimative of the linear mode coupling taking place along a FMF. More importantly, using the semi-analytical method the computation time required to calculate the linear coupling along a fiber with a few meters is reduced by three orders of magnitude compared to the RK45 method which required tens of seconds executing on a standard personal computer operating at 2.8GHz.

In conclusion, the semi-analytical solutions obtained enable a time efficient and accurate computation of the linear coupling occurring along the fiber length. They are therefore a valuable alternative to the numerical solution, which would not be practical due to computation time constraints.

10.5 MULTI-SECTION MODELLING

We propose a multi-section model were the coupling strength is set using a given radial displacement and a uniformly distributed azimuthal displacement for each section. The radial displacement to be used depends not only on the target coupling strength but also on the fiber step length to be used. But first we quantitatively define the mode coupling strength and present its dependence on the radial displacement.

10.5.1 *Setting Mode Coupling Strength and Correlation Length*

The statistical nature of polarization mode dispersion (PMD) in SMFs is mainly determined by the correlation length, which is defined in terms of fiber mode coupling. In SMFs, the mode coupling is easily defined as there is only two polarizations, and the L_c is defined as the length for which the average power in the orthogonal polarization is within e^{-2} of the power in the launching polarization. In FMFs, the mode coupling strength can be quantified as the ratio between the average power in all the other orthogonal modes and average power remaining in the launching mode, after a certain distance. Thus, there are as many coupling strength values and L_c as the number of modes. Inevitable, the fiber mode m showing higher coupling strength will set an important reference for the study of the mode group-delay statistics. Finally, the mode coupling strength definition for FMFs is:

$$XT_m = \sum_{v \neq m}(P_v \,/\, P_m), \tag{20}$$

where P_v is the power of mode v, after a given fiber segment under test, when only the m mode was launched, where m is the mode that shows higher coupling strength. In the FMF case, we generalize L_c for mode m as the length for which $(P_m - \sum_{v \neq m} P_v) = e^{-2}$, this is $XT_m = [e^2 - 1]/[e^2 + 1]$ (-1.18 dB).

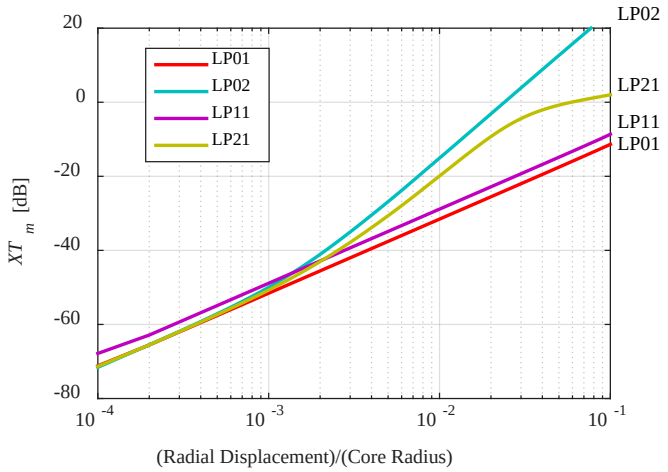

Figure 5. XT_m averaged over the azimuth displacement as a function of the radial displacement.

In our multi-step model a given amount of coupling is set by selecting a fixed amount of radial displacement and selecting a random azimuth displacement given by a uniform distribution. In this way, the proposed model introduces a random amount of crosstalk per step that in average approximates the desired level. Fig. 5 shows the *mode coupling strength* averaged over the azimuth displacement, as a function of the normalized radial displacement, for a 6 LP mode fiber presented in Section 10.4. Note that, coupling strengths are calculated considering degenerate modes such as LP_{11a} and LP_{11b} as one mode, e.g. $XT_{LP11a,b}$ equals to $\sum_{v \neq LP11a,b}\{P_v / (P_{LP11a}+P_{LP11b})\}$. In Fig. 5, the mode coupling strength only depends significantly on the mode being considered for displacements higher than 1 %. Such higher coupling for LP_{02} and LP_{21} can be explained noting they belong to the same LP mode group. Moreover, $XT_{LP21} \leq XT_{LP02}$ for any displacement in Fig. 5 because any power launched in LP_{21a} couples preferentially with LP_{21b} (and vice-versa) and in the second place to LP_{02}. Given the higher values of XT_{LP02}, we define L_c for this mode. Note that XT_m values above 10 dB mean that almost all power launched in mode m has been transferred to other modes.

In the literature, the mode coupling values of fabricated FMFs range from -50 dB/100m to -40 dB/100m for fibers with step-index or graded-index profiles [20, 21], going up to -28 dB/100m for coupled multi-core fibers [22] and -7 dB/100m for fibers with ring-index profiles [23].

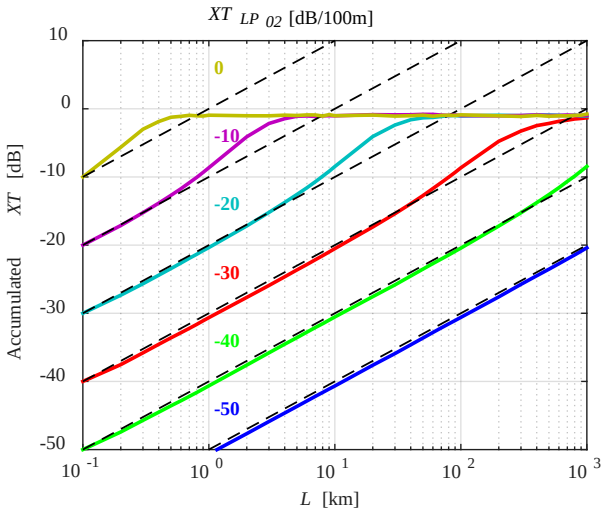

Figure 6. Accumulated XT as a function of the fiber length, for different coupling strength, averaged over 10,000 runs.

10.5.2 *Mode Coupling Accumulation over Transmission Length*

In a multi-section model, the mode coupling accumulates section after section in such a way that in average should follow the same continuous growing function that was first derived to describe the accumulation of polarization coupling in polarization-maintaining fibers [35]:

$$XT = \tanh(hz) \tag{21}$$

where h is the mode coupling parameter (measured in m^{-1} units) and z is the fiber length.

To validate our multi-section model, we have run 10,000 transmission simulations considering the 6-mode fiber presented in Section 10.4. Fig. 6 shows the average XT_{LP02} as a function of the fiber length (L) from 10 m to 1000 km, considering a fiber section of 10 m and different values of coupling strength. Note that the dashed lines in Fig. 6 represent the evolution predicted for (21) using the respective h coefficient. A very good agreement between the proposed multi-section model and (21) is noticeable. Furthermore, similar matches were obtained for other section sizes and respective radial displacements.

10.5.3 *Polarization Mode Coupling*

After a few meters, the two nearly degenerate polarization modes of each spatial mode strongly couple to each other and the FMF enters the polarization coupling state [4, 31]. Such propagation mode coupling can be described by a block diagonal matrix with a sequence of $M/2$ submatrices along the diagonal. Each of these 2×2 random unitary submatrices is a PMD transfer matrix [4].

The full coupling matrix for the i^{th}-section is modelled as the product of two matrices: one block diagonal matrix describing the polarization mode coupling, and one matrix describing finite inter- and intra-mode group coupling (as described in Section 10.3 10.4, and 10.5). This approach follows a similar reasoning to that in [4, 24] to deal with coupling processes having different correlation lengths.

10.6 GD STATISTICS IN NON-DELAY-MANAGED LINKS

In previous work [36], it has been shown that the approach of considering principal states of polarization (PSPs) with well-defined GDs in SMFs, can be extended to FMFs. In FMFs, the coupled modes having well defined GDs are called principal modes (PMs). In both cases the statistics of the GDs are dependent on the linear coupling strength, thus the correlation length L_c. The coupling regimes may then be broadly defined as strong coupling when $L >> L_c$, weak coupling when $L << L_c$, and intermediate coupling otherwise. In the FMF case, the statistical properties of the GDs are well known for the two extreme regimes [4, 11-14]. In the weak coupling regime, the GD spread grows linearly with distance and in the strong coupling regime grows with the square root of the distance. In the intermediate coupling regime, we have shown in [27] through simulation that the GDs statistics in SMFs can be extended to FMFs, at least for fibers guiding 3 LP modes. At the same time, the complete analytical derivation of such extension was presented in [37].

The temporal spread of propagating pulse is determined by the modal dispersion (MD) vector $\boldsymbol{\tau}$, as defined for a generalized (M^2 - 1)-dimensional Stokes space in [13] (M modes). Knowledge of the MD vector allows the extraction of the PMs and respective GDs as explained in [13]. Moreover, the square modulus of the MD vector is proportional to the sum of the GDs τ_i (with $\sum \tau_i = 0$) [13]:

$$\|\boldsymbol{\tau}\|^2 = M\sum_{i=1}^{M}\tau_i^2 \tag{22}$$

In this way, it can be noted that $\|\boldsymbol{\tau}\|/M$ is the standard deviation of the GD vector $[\tau_1, \tau_2, \ldots\tau_M]$, σ_{gd}. The MD vector has been used to explicitly determine the delay spread T in two limiting cases: one in which the PMs change rapidly across the signal bandwidth, and one in which the bandwidth of the PMs is much larger than the signal bandwidth. In the first case, T is a deterministic quantity and determined by σ_{gd}, $T^2 = E\{\|\boldsymbol{\tau}\|^2\}/M^2 = E\{\sigma_{gd}^2\}$ 0, where $E\{\cdot\}$ denotes expectation. In the latter case, T is a random quantity given by $\max_i\{\tau_i\} - \min_i\{\tau_i\}$ [11, 13], determined by the GD PDF.

In the following, we review the known MD statistics and use them to validate the multi-section model proposed in Section 10.5 for a fiber guiding 6 LP modes despite the different coupling strengths between different pairs of modes belonging to different mode groups. The FMF presented in Section 10.4 is considered again, the modal and chromatic dispersion values are given in Table 1. The fiber presents a DMD of 5.19 ps/km and we assumed zero DMD between degenerate LP modes and between orthogonal polarizations. As explained in Section 10.5.2, the polarization mode coupling is considered in each section using a block diagonal matrix. Regarding the coupling matrix describing finite inter- and intra-mode group coupling, the XT_{LP02} value was varied from -50 to 0 dB/100m by using a given radial displacement and a uniformly distributed azimuthal displacement for each section (see Fig. 5), assuming a section length of 10 m. This range fully covers the range of coupling values presented in the literature [20-23]. Finally, the GDs of the PMs are the eigenvalues of the semi-analytically simulated transmission matrix. Note that the simulated transmission matrix must be compensated for chromatic dispersion as introduced by (3).

10.6.1 *GD Standard Deviation and Intensity Impulse Response*

Knowledge of the modulus of the MD vector $\|\boldsymbol{\tau}\|$ allows to determine the standard deviation of the GD vector $[\tau_1, \tau_2, \ldots\tau_M]$ σ_{gd}, since $\sigma_{gd} = \|\boldsymbol{\tau}\|/M$. $E\{\|\boldsymbol{\tau}(z)\|^2\}$ can be found by integration of two deterministic differential equations (z dependence is omitted)[5, 37]:

$$\partial_z E\{\|\boldsymbol{\tau}\|^2\} = E\{2\partial_\omega\boldsymbol{\beta}\,\boldsymbol{\tau}\} = 2\partial_\omega\boldsymbol{\beta}\,E\{\boldsymbol{\tau}\} \tag{23.1}$$

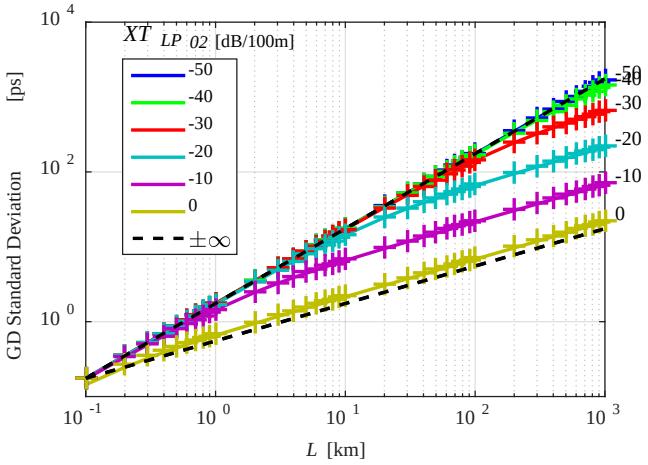

Figure 7. Standard deviation of the GDs of the PMs as a function of transmission distance showing simulation results (markers) and analytical results (solid lines).

$$\partial_z E\{\boldsymbol{\tau}\} = \partial_\omega \boldsymbol{\beta} - 1/L_c \, E\{\boldsymbol{\tau}\} \tag{23.2}$$

where $\partial_\omega \boldsymbol{\beta}$ term represents the uncoupled GDs per unit length and L_c is the correlation length characteristic of the fiber, considering the same L_c for all groups of modes.

For non-DMD-managed spans (this is, $\partial_\omega \boldsymbol{\beta}$ constant), $E\{\| \boldsymbol{\tau}(z) \|^2\}$ can be found through analytical integration of (23), and is given by [5, 37]:

$$E\{\| \boldsymbol{\tau} \|^2\} = 2 \| \partial_\omega \boldsymbol{\beta} \|^2 L_c^2 (e^{-z/L_c} + z/L_c - 1) \tag{24}$$

Equation (24) was proposed and validated by simulation in [27] for fibers guiding 3 LP modes, and at the same time its analytical derivation being presented in [37].

Fig. 7 shows the standard deviation of the GD vector ($[\tau_1, \tau_2, \ldots \tau_{12}]$) as a function of distance up to 1,000 km, obtained by averaging over 6,000 different realizations of lateral offsets giving rise to a given XT_{LP02} value. These results were obtained using the fiber presented in Table 1, treating the polarization mode coupling as described in Section 10.5.2. Fig. 7 shows a good agreement between simulation and (24), for any coupling value studied and for any distance up to 1,000 km (even 10,000km has further results shown). Similar agreement between (24) and simulation results has been presented in Fig. 3 of [5]. This provides mutual

validation of (24) and the proposed multi-section model proposed. In Fig. 7, for coupling values ranging from -50 to -40 dB/100m, σ_{gd} scales approximately linearly with distance. But, at -40 dB/100m the deviation from linear growth is already noticeable around 1,000 km, thus even with such a low coupling, the FMF is operating in intermediate coupling regime. Increasing XT_{LP02}, σ_{gd} gradually converges to the strong coupling regime. However, even for a XT_{LP02} equal to -7.01 dB/100m (the highest value found in literature [23]), the fiber is still not well modelled by random unitary matrices every 100 m, it would underestimate σ_{gd} by a factor of 2.76.

For FMFs where the PMs change rapidly across the signal bandwidth, MD can be conviniently characterized by exciting each spatial channel (one at a time) with a short optical pulse and measuring the received intensities in each of the output spatial channels. Such process leads to $M \times M$ intensity waveforms, whose sum $I(t)$ has been used to assess the signal delay spread caused by MD [5, 14]. For strong mode-coupling and typical MD values, it has been shown that $I(t) = r(t) * I_0(t)$ [14], where $*$ represents convolution, $I_0(t)$ is the launching signal intensity waveform, and $r(t)$ is FMF's intensity impulse response (IIR). Also in [14], it was shown theoretically and experimentally that $r(t)$ is a Gaussian function with variance equal to $T^2 = E\{\|\boldsymbol{\tau}\|^2\}/M^2 = E\{\sigma_{gd}^2\}$, thus:

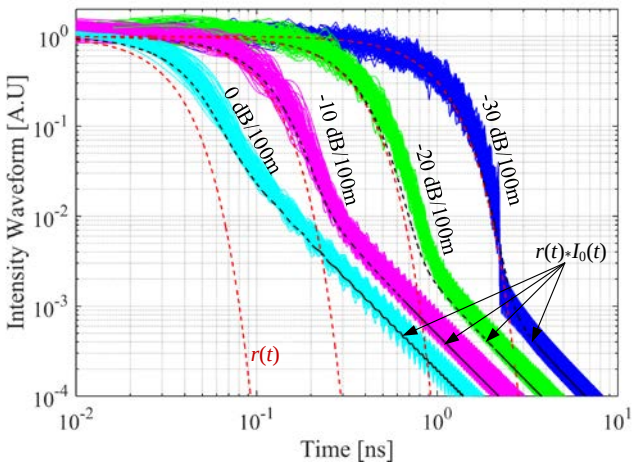

Figure 8. Mode-averaged intensity waveform for different coupling values after transmission of a Nyquist signal. Simulation results, $r(t)*I_0(t)$ and $r(t)$ plotted using colored full lines, black dashed lines and red dashed lines, respectively.

$$r(t) = \frac{1}{\sqrt{2\pi T^2}} \exp\left(\frac{-t^2}{2T^2}\right) \tag{25}$$

Equation (25) is valid as long as the correlation bandwidth ($B_{MD} = 1/2\pi T$) of the fiber transfer matrix is much smaller than the channel bandwidth ($B \sim$ tens of GHz). Fig. 8 shows the mode-averaged intensity waveform for $M = 12$ modes after transmission of a Nyquist signal $I_0(t) = \sqrt{B}\sin(\pi Bt)/(\pi Bt)$, with $B = 20$ GHz, over a 1000km link with coupling values ranging from -30 to 0 dB/100m. Simulation results, $r(t)*I_0(t)$ waveform, and $r(t)$ IIR are plotted using colored full lines, black dashed lines, and red dashed lines, respectively. Fig. 8 displays simulation results for 100 different fiber realizations for each XT_{LP02} value. All the waveforms were normalized so that their peak value is one. Fig. 8 shows an excellent agreement between simulations and theory (experimentally validated) as obtained in [14]. Note that the deviations from theory reduce as the coupling strenght increases and the PMs bandwidth decreases. Finally, further results show that the deviation of $T(z)$ from theory is in agreement with the theory in [14].

10.6.2 *GD Probability Density Function and Maximum GD Spread*

The probability density function (PDF) of the GDs has been derived analytically for strong coupling [11] where the coupling matrix can be described as a Gaussian unitary ensemble. The ordered joint pdf of the eigenvalues (τ_i) of a $M \times M$ Gaussian unitary ensemble with zero trace ($\sum \tau_i = 0$) is:

$$p_M(\tau_1, ..., \tau_{M-1}) = \rho_M \prod_{M \geq i > j > 0} (\tau_i - \tau_j)^2 e^{\left(-\sum_{i=1}^{M} \tau_i^2\right)} \tag{26}$$

with order constrain $\tau_1 \leq \tau_2 \leq \ldots \leq \tau_M$ and where the constant ρ_M is defined by requiring (26) to integrate to unity. The unordered joint PDF is just $1/M!$ of (26) but without the order constraint. In this way, the marginal PDF of τ is can be obtained by integrating over $\tau_2, \ldots, \tau_{M-1}$:

$$p_{M\tau}(\tau) = \frac{1}{M!} \int_{-\infty}^{+\infty} \ldots \int_{-\infty}^{+\infty} p_M(\tau, \tau_2, ..., \tau_{M-1}) d\tau_2 ... d\tau_{M-1} \tag{27}$$

Analytical solutions of (27) can be find in [4, 11] for any M.

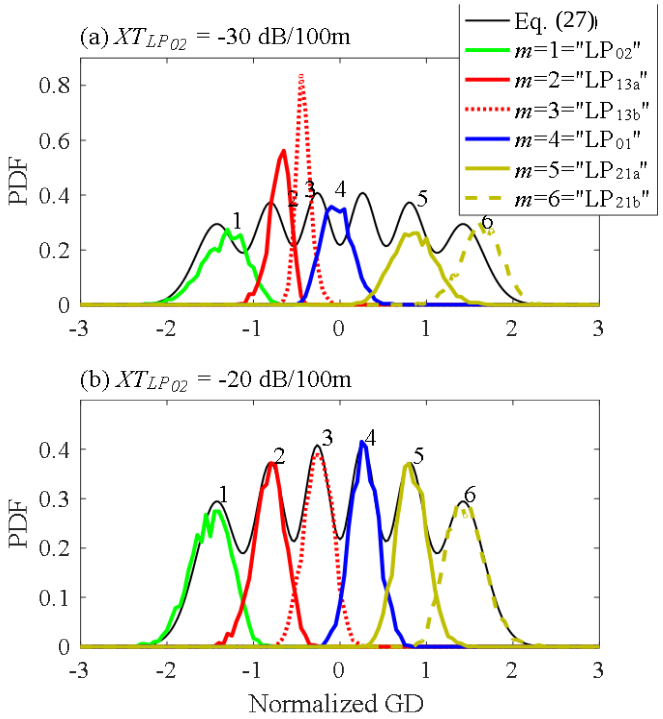

Figure 9. Probability density function of the ordered normalized GDs (τ_m/σ_{gd}), obtained through simulation after 1000 km, with different XT_{LP02} values.

Fig. 9 shows the PDF of the ordered GDs (τ_m, $\tau_1 \leq \tau_2 \leq \ldots \leq \tau_6$) obtained for 6000 different fiber matrix realizations, normalized by the σ_{gd}, after 1000 km for two different coupling values, overlapped with the analytical joint PDF (thin black line) derived for the strong coupling regime (27). Note that the normalization factor (σ_{gd}) depends on the XT_{LP02} (L_c) value, see (24). Exceptionally, these results were obtained for single-polarization to facilitate the visualization of the individual GDs evolution in Fig. 9, but similar matching between simulation and theory was obtained when considering dual-polarization. Fig. 9 (a) shows that for -30 dB/100m the GDs of the PMs vaguely resemble the GDs of the LP modes given the impulse-like PDF of τ_2 ("LP_{11a}") and τ_3 ("LP_{11b}"). Further results for lower coupling values shown that all GDs present impulse-like PDFs. In Fig. 9 (b), for -20 dB/100m, the match between the simulated PDFs and the analytical PDF for strong coupling is good, even though the GDs have been normalized by different factors (24). Further

increase of the coupling strength leads to improved matching between the simulated PDFs and the analytical PDF, as observed in additional results.

In a MDM system for which the bandwidth of the PMs is much larger than the signal bandwidth, the digital equalizer must span a temporal memory at least as long as the the difference between the maximum and the minimum group delay $(\tau_M - \tau_1)_{total}$. As shown in [12], the probability of having a GD spread lower than x, $P(\tau_M - \tau_1 \le x)$ – the cumulative distribution function, can be computed as a function of the joint probability of having all eigenvalues falling within an arbitrary interval $[x, y]$, $P(\tau_M \le x, \tau_1 \ge y)$, this is:

$$P(\tau_M - \tau_1 \le x) = -\int_{-\infty}^{+\infty} \partial_y P(\tau_M \le y + x, \tau_1 \ge y) dy \tag{28}$$

$$P(\tau_M \le x, \tau_1 \ge y) = \int_y^x \dots \int_y^x p_M(\boldsymbol{\tau})\, d\tau_1 \dots d\tau_M \tag{29}$$

According to [12], (27)-(29) can be evaluated using at least three methods: Fredholm determinant, Andréief identity or one approximation based on Tracy–Widom distribution. Finally, from (27), we can obtain the equalizer memory length x required to accommodate the GD spread with a given outage probability p, this is: $P(\tau_M - \tau_1 > x) = p = 1 - P(\tau_M - \tau_1 \le x)$.

Fig. 10 shows the complementary cumulative distribution function (CCDF) of the normalized GD spread, $P[(\tau_6 - \tau_1)/\sigma_{gd} > p]$, obtained through simulation after 1000 km for different coupling values (averaging over 6000 different realizations). These results were obtained for single-polarization to be consistent with the PDFs in Fig. 9. Fig. 10 shows that for $XT_{LP02} \ge$ -30 dB/100m the CCDFs are very similar to the analytical approximation obtained for strong coupling (28) (dashed line). Conversely, for XT_{LP02} lower than -30 dB/100m the normalized GD spread is significantly smaller than the normalized GD spread for strong coupling. Finally, we can conclude that the required temporal equalizer memory length (in time units) to span a channel with an outage probability smaller than 10^{-4} is equal to $4.5\sigma_{gd}$, for any coupling strength, where σ_{gd} depends on the mode coupling strength, see (24).

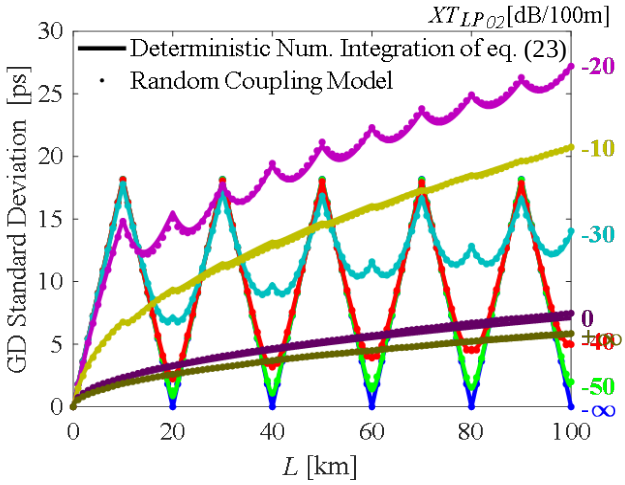

Figure 11. Standard deviation of the GDs as a function of the propagation distance, for fibers with a compensation length of 20 km and different values of coupling strength.

10.7 GD STATISTICS IN DELAY-MANAGED LINKS

In differential mode delay (DMD) managed spans, GD spread is reduced by cascading fibers with opposite sign DMD. In the absence of mode coupling, the GD spread at the end of the span would be zero. However, in the presence of coupling, the DMD compensation is no longer fully effective. In order to minimize the impact of coupling, the length of the segments over which DMD sign is inverted has to be made much smaller than the correlation length set by the coupling, L_c.

To compensate for linear mode coupling and group delay spread, MIMO-DSP can be used, but DSP complexity increases with the number of modes and the total GD spread. In order to minimise complexity, the total GD spread should typically be reduced to less than 10 ns [38].

For DMD-managed spans, where uncoupled GDs (per unit length) $\partial_\omega \boldsymbol{\beta}$ are a piecewise constant function of z a general analytical solution of (23) for $E\{\|\boldsymbol{\tau}(z)\|^2\}$, rapidly becomes too complex as the number of fiber segments increases. Therefore, numerical integration should be performed as in [37].

In order to verify the deterministic numerical integration of (23) we made use of the multi-section model presented in Section 10.5. The simulations considered that each span of length L comprised S segments,

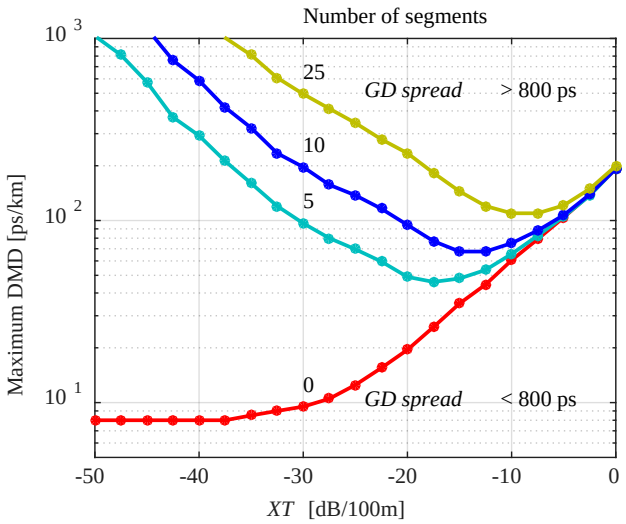

Figure 12. Contour plot of the pairs (*DMD*, *XT*) that allow for a GD spread lower than 800 ps after 100 km with a probability higher than 95 %.

where each segment was itself composed by two fibres of length $L/S/2$ with the same characteristics but opposite sign GD. The first fibre is the same presented in Section 10.5. The second fibre is not obtained through optimization but just by negating the GD vector, keeping the remaining characteristics of the first fibre. Finally, to make analysis straightforward DMD value is sweep by scaling the GD vector in Table 1 as required after normalization by the highest GD value in the vector.

Fig. 11 shows the evolution of the standard deviation of the GD vector ($[\tau_1, \tau_2, \ldots \tau_{12}]$) with propagation distance, assuming compensation length of 20 km (10 km with the positive GD vector followed by 10km with the negative GD vector), for different values of coupling strength. In Fig. 11, there are two sets of results, one obtained for transmission using the proposed multi-section model (dot markers) and one given by the deterministic numerical integration of (23) (full lines). A section length of 10 m was used as smaller section lengths generated similar results. In Fig. 11, we can observe a very good match between the deterministic numerical integration and the proposed multi-section model. It can be inferred from these results that the semi-analytical solutions in Section 10.4 multi-section model in Section 10.5 are accurate under any coupling regime for DMD managed links.

In order to study a broader range of DMD scenarios, the GD vector was normalized by the highest GD value in the vector. Fig. 12 shows the combinations of (*DMD*, *XT*) that allow for a GD spread lower than 800 ps after 100 km with a probability higher than 95 %. In Fig. 12, for a given span configuration, GD spread is lower than 800 ps for (*DMD*, *XT*) pairs below the respective curve. For non-DMD-managed spans, the maximum tolerable DMD increases with the coupling strength, being very low for weak coupling. For DMD-managed spans, as the number of segments increases, increasingly high DMD values are tolerable for weak coupling. For higher levels of coupling (above -20 dB/100m), the tolerable DMD converges to that of the non-DMD-managed spans. Importantly, the tolerable DMD for the DMD-managed spans is always greater than or equal to the non-DMD-managed spans.

10.8 NONLINEAR PROPAGATION MODELLING

The generalized nonlinear Schrödinger equation (GNLSE) for FMFs can be written as [7, 8, 17]:

$$\overbrace{\partial_z A_{ui} + \left(\beta_{ui}^{(1)}\partial_t - \frac{\mathrm{j}\beta_{ui}^{(2)}}{2}\partial_t^2 + \ldots + \frac{\alpha_{ui}}{2}\right)A_{ui}}^{=\hat{D}} = \overbrace{-\mathrm{j}\Big[\gamma_{uuii}\left|A_{ui}\right|^2 + 2\gamma_{uvii}\sum_{v\neq u}\left|A_{vi}\right|^2 + \frac{2}{3}\gamma_{uvij}\sum_{v}\left|A_{vj}\right|^2\Big]A_{ui}}^{=\hat{N}} - \mathrm{j}\sum_{vk} C_{uvik}A_{vk}e^{\mathrm{j}\left(\beta_{ui}^{(0)}-\beta_{vk}^{(0)}\right)z} \tag{30}$$

where i and j are the orthogonal polarizations of mode u. $A_{ui}(z,t)$, $\beta_{ui}^{(1)}$, $\beta_{ui}^{(2)}$ and a_{ui} are the slowly varying field envelope, GD, GD dispersion and attenuation, respectively. γ_{uvij} is the nonlinear coefficient between ui and vj, which depends on the intermodal effective area as shown in [17]. In (30), $\hat{D}$ is the differential operator that accounts for dispersion and attenuation, and $\hat{N}$ is the nonlinear operator that accounts for all the intramodal and intermodal nonlinear effects [17]. The last term on the right-hand side accounts for the linear mode coupling arising from fiber structure imperfections, where C_{uvij} are the coupling coefficients as derived in [6].

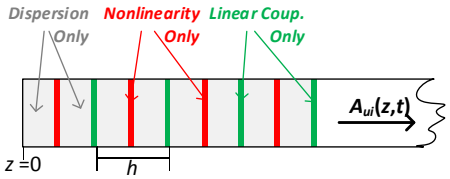

Figure 13. Schematic illustration of the symmetric SSFM used for numerical simulations.

10.8.1 *Modified Split-Step Fourier Method*

To numerically solve (30), we use a modified version of the split-step Fourier method (SSFM) developed for SMFs. In the SMF case, an approximate solution of the Schrödinger equation is obtained by assuming that over a small distance h the dispersive and nonlinear effects act independently. For FMFs, we extend such an approach by assuming that the mode coupling also acts independently. Such approximation requires h to be much shorter than: the dispersion length $T_0^2/|\beta_u^{(2)}|$, the walk-off length $T_0/|\beta_u^{(1)}-\beta_v^{(1)}|$ (T_0 is the pulse width), and the correlation length L_c defined in [6] such that $XT(L_c) = [e^2 - 1]/[e^2 + 1]$.

To include the linear mode coupling, the SSFM is now modified to include an additional step. Fig. 13 presents a schematic illustration of the symmetric SSFM considered for numerical simulations in this paper. By using a symmetric SSFM, the effect of nonlinearity is included in the middle of the segment rather than at the segment boundary providing higher accuracy [39]. Finally, the step-size was selected by bounding the local error [39], more computationally efficient at high accuracy than the other methods, e.g. nonlinear phase rotation.

10.8.2 *Extreme Coupling Strength Regimes*

In the presence of extreme mode coupling strength (weak or strong), it has been shown that the nonlinear distortion can be modelled using averaged coefficients instead of explicitly considering and solving for random coupling matrices. In [7, 8], new Manakov equations were derived for FMFs.

In the weak-coupling (WC) regime [8], it has been found that only the averaging over birefringence fluctuations must be considered, reducing

the intramodal degeneracy factor to 8/9 and the intermodal degeneracy factor to 4/3.

$$\hat{N} = -\mathrm{j}\left[\frac{8}{9}\sum_{k=\{i,j\}}\gamma_{uuik}\left|A_{uk}\right|^2 + \frac{4}{3}\sum_{\substack{v\neq u\\ k=\{i,j\}}}\gamma_{uvik}\left|A_{vk}\right|^2\right] \tag{31}$$

In the strong coupling (SC) regime [7, 8], the averaging must include all propagation modes. For N-modes, the nonlinear operators for WC and SC are, respectively [7, 8]:

$$\hat{N} = -\mathrm{j}\sum_{\substack{v\\ k=\{i,j\}}}\kappa\left|A_{vk}\right|^2, \quad \kappa = \frac{4}{3}\frac{2N}{2N+1}\left(\frac{1}{N^2}\sum_{\substack{u,v\\ k,l=\{i,j\}}}\gamma_{uvkl}\right) \tag{32}$$

10.8.3 *Intermediate Coupling Strength Regime*

In the intermediate coupling regime, (30) must be solved explicitly applying every step new random matrices characteristic of a given coupling strength. In [6], the authors proposed a semi-analytical solution method for the coupled linear differential equations that describe the linear modal coupling in FMFs, this is a solution of (30) assuming the linear mode coupling acting independently as explain in Section 10.8.1, the linear mode coupling step in Fig. 13. The semi-analytical solution method [6] has been proved accurate in the linear power regime. It accurately matched the analytical predictions for the statistics of GDs in FMF links for different transmission lengths 10 m-to-10,000 km, in any coupling regime -50 dB/100m to 0 dB/100m, without and with group delay management. For convenience, the mode coupling strength (XT) is quantified taking the LP01 mode as reference, this is: $XT=\sum_{n\neq LP01} P_n/P_{LP01}$ where P_n is the power of mode n, after a given segment under test, when only mode $LP01$ was launched.

Here, we use the semi-analytical model [6] to implement the linear mode coupling step in Fig. 13. Using this method, the accuracy of full stochastic solutions of (30) will be compared with different analytical expectations, regarding the total nonlinear noise and the nonlinear transmission performance of quadrature amplitude modulated signals.

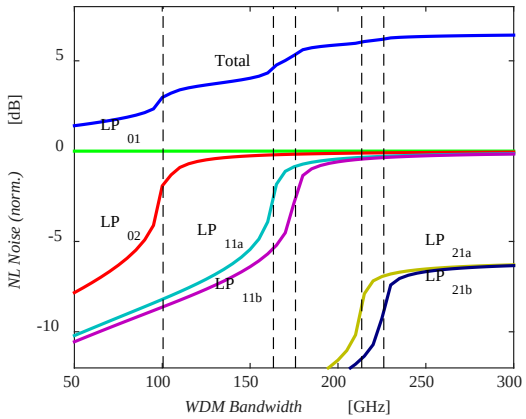

Figure 14. Contribution to the nonlinear noise power in the LP_{01} mode for signals propagating in higher order modes normalized by the LP_{01} intra-modal nonlinear noise power, as a function of WDM bandwidth.

10.8.4 *Total Nonlinear Noise: Analytical Integration*

The total nonlinear noise generated can be analytically calculated using a generalization of SMFs four-wave mixing (FWM) theory to FMFs [40]. This is, when considering three waves denoted p, q, r propagating in modes denoted a, b, c, respectively, the nonlinear signal A_{ds} generated at angular frequency $\omega_s = \omega_p + \omega_q - \omega_r$ in mode d is:

$$A_{ds} = \xi_{abcd} A_{ap} A_{bq} A_{cr}^{*} \frac{1-e^{-\alpha L} e^{-\mathrm{j}\Delta\beta_{abcd} L}}{\mathrm{j}\Delta\beta_{abcd,pqrs} L+\alpha} \cdot e^{-\alpha/2 L} e^{-\mathrm{j}\beta_{ds} L} \tag{33}$$

where α is the attenuation and L is the span length. ξ_{abcd} is the total nonlinear coefficient between modes a, b, c, d given by the product of γ_{abcd} and the degeneracy factor dependent on the coupling strength (30)-(32). $\Delta\beta_{abcd,pqrs}$ is the phase mismatch between waves p, q, r, s. The phase mismatch is given by $\Delta\beta_{abcd,pqrs} = \beta_{ap} + \beta_{bq} - \beta_{cr} - \beta_{ds}$ where β_{ap} is the propagation constant of mode a at angular frequency ω_p.

Finally, assuming an optical super-channel with a total bandwidth B the total nonlinear noise between a given set of modes can be calculated by integrating the product of (33) with the signal power spectral density (PSD) in each mode. A closed form solution for this integral was obtained (and experimentally validated) for the case of a signal with a

rectangular spectrum (OFDM or Nyquist WDM super channel) in each interacting mode, and the overall efficiency parameter η_{abcd} was shown to be [40]:

$$\eta_{abcd} = \frac{\gamma_{abcd}^2}{\pi\alpha\left|\beta^{(2)}\right|}\left[\ln\left(\frac{B^2+2B\Delta f_{abcd}}{2f_w}\right) + s\ln\left(s\frac{B^2-2B\Delta f_{abcd}}{2f_w}\right)\right], \quad (34)$$

where $\Delta f_{abcd} = \left(\beta_a^{(1)} + \beta_b^{(1)} - \beta_c^{(1)} - \beta_d^{(1)}\right)/2\pi\beta^{(2)}$, $s = \text{sign}(B - 2\Delta f_{abcd})$, $f_w = \sqrt{\alpha/4\pi^2\left|\beta^{(2)}\right|}$, $\beta_a^{(1)}$ is the group delay of mode a, $\beta^{(2)}$ is the second-order dispersion coefficient, and Δf_{abcd} is the velocity-matched frequency offset. In the derivation of (34) it is assumed that [40, 41]: the second-order dispersion coefficient $\beta^{(2)}$ is mode independent; mode group velocities $\beta_a^{(1)}$ are frequency independent; given large $\beta_a^{(0)}$ differences, strong inter-mode phase-matching is only possible for interactions of pairs of modes ($a = d, b = c$ or $b = d, a = c$). According to (34), the FWM efficiency is maximized for frequency offsets Δf_{abcd} at which the walk-off induced by chromatic dispersion and the walk-off induced by mode delay cancel out exactly. Finally, the total nonlinear power generated in mode d is given by $\left(\sum_{a,b,c}\eta_{abcd}\right)P_aP_bP_c$, where P_a is the signal power spectral density in mode a.

Fig. 14 shows the nonlinear noise power generated at the center of the WDM signal as a function of the overall bandwidth (B) for a particular six linearly polarized (LP) mode fiber with no linear mode coupling. In addition to the logarithmically increasing background expected for a SMF [42], a number of discontinuities are apparent whenever B becomes sufficiently large to allow strong phase matching among an additional pair of modes. In Fig. 14, the dashed vertical lines identify these discontinuities ($B/2 = |\Delta f_{abcd}|$). To enhance the visualization of all possible phase matchings, the results in Fig. 14 were obtained with an arbitrary GD vector: (0, 8, 13, 14, 17, 18) ps/km for (LP_{01}, LP_{02}, LP_{11a}, LP_{11b}, LP_{21a}, LP_{21b}), respectively. All the other fiber characteristics follow Table 1.

10.9 LINEAR COUPLING IMPACT NONLINEAR NOISE FOR DELAY UNCOMPENSATED SPANS

In this section, the nonlinear noise power is found by solving (30) for a range of different linear coupling strengths ranging from the weak to the strong coupling regimes using the modified SSFM presented in Section

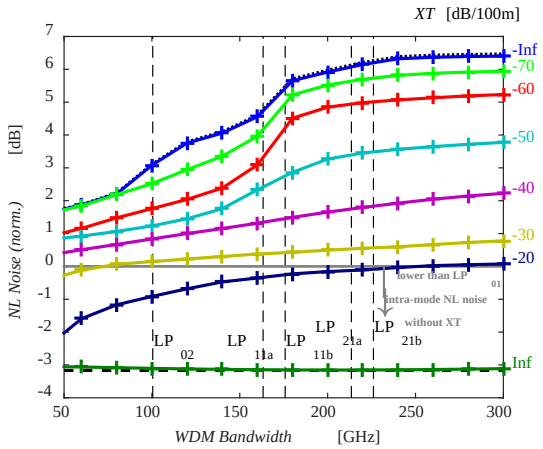

Figure 15. Total nonlinear noise power in the LP_{01} mode as a function of WDM bandwidth showing analytical predictions from strong (dashed) and weak (dotted) regimes along with numerical simulations (solid) for different mode coupling strengths (colors).

10.8, and by using (34). The simulations assume an optical super-channel with: a rectangular power spectral density (e.g. OFDM), a total WDM bandwidth B, and a subcarrier spacing of 50 MHz (smaller spacing generated similar results). The XT value was varied from -70 to 0 dB/100m covering all coupling values presented in the literature. To the best of our knowledge, the lowest XT values reported are around -50 dB/100m [20] and the highest XT value reported is -7 dB/100m [23]. Finally, simulations considered the same fiber characteristics as used in Fig. 14.

Fig. 15 shows the nonlinear noise power at the center frequency of the WDM band carried by the LP01 mode versus the total WDM bandwidth. The modified SSFM step size was selected by bounding the local error to be lower than 10^{-5} (smaller local errors generated similar results). The simulation results in Fig. 3 lay between two analytical lines obtained with (34) using: the ordinary fiber nonlinear coefficients (for weak mode coupling) [8], dotted line, and using the average nonlinear coefficients derived in [7] for strong mode coupling, dashed line. It can be noted in Fig. 15 that the rate of decrease of the nonlinear noise with XT increasing is higher for larger bandwidths than for smaller bandwidths, which shows that the averaging of the nonlinear coefficients among the higher-order modes occurs more rapidly. For small values of XT, -70

and -60 dB/100m the steps associated with the inter-mode interactions of LP_{01} with LP_{02} and LP_{21a}/LP_{21b}, become smooth, but the step associated with LP_{11a}/LP_{11b} remains unchanged. This is in line with the asymmetries on the coupling strength between pairs of modes from the same mode groups (stronger) and from different mode groups (weaker) (modes LP_{02} and LP_{21a}/LP_{21b} belong to the same mode group). Increasing *XT* up to -40 dB/100m, smooths the step associated with inter-mode interactions of LP_{01} with LP_{02}. Furthermore, increasing *XT* above -20 dB/100m reduces nonlinear noise power below the LP_{01} intra-mode nonlinear noise power in the absence of linear coupling which was used to normalize the results. In the limit, strongly coupling all modes, using unitary matrices every 10 m (and shorter steps, as verified), the nonlinear noise power matches the analytical results (dashed line) obtained with (34) and the average nonlinear coefficients in [7].

In conclusion, for the crosstalk values shown by the majority of FMFs (from -50 to -20 dB/100m), the nonlinear noise is not accurately estimated by either the weak linear coupling regime or the strong coupling regime. However, the overall conclusion that the stronger coupling reduces nonlinear noise power remains valid. Finally, the reduction of nonlinear noise below that of uncoupled single-mode propagation for linear coupling requires *XT* values above -20dB/100m.

10.10 LINEAR COUPLING IMPACT ON NONLINEAR NOISE FOR DELAY COMPENSATED SPANS

In this section, we revisit the GD managed spans studied in Section 10.7, to analyze their nonlinear performance. As mode delay compensation is used and the GD spread is reduced, the total nonlinear noise is expected to increase as phase matching becomes possible for smaller WDM bandwidths.

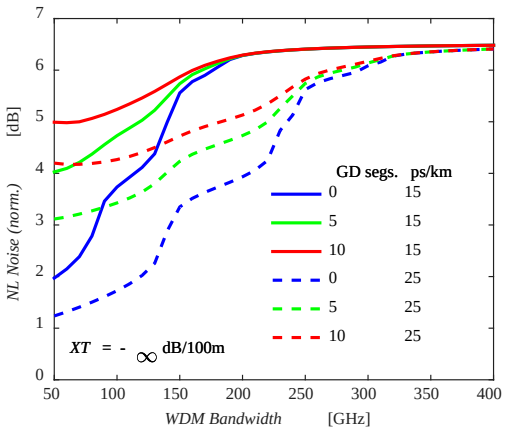

Figure 16. Total nonlinear noise power in the LP_{01} mode as a function of WDM bandwidth, for [0 5 10] compensation segment for DMD [15 25] ps/km, and no XT.

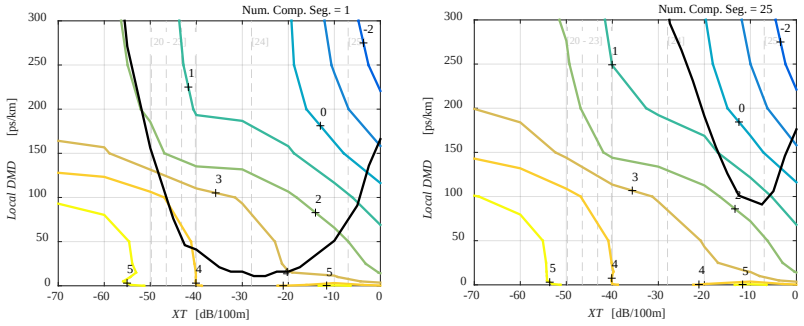

(a) (b)

Figure 17. Contour plots of the nonlinear noise power in the LP_{01} mode, as a function of mode coupling strength and DMD, normalized by the LP_{01} intra-modal nonlinear noise power (normalized noise values are in dB). Four DMD maps are considered: (1) 1 segment, and (b) 25 segments.

Fig. 16, shows the impact of mode delay compensation on the total nonlinear noise, in the absence of linear mode coupling, simulations considered the same fiber characteristics as used in Fig. 14 with different GD vector scaling for each *DMD* value. We can see that when the WDM bandwidth is small enough such that not all phase matching conditions are meet, the introduction of mode delay compensation increases the total nonlinear noise comparing with the non-compensated case. But if the WDM bandwidth is such that already satisfies all possible phase

matchings for non-compensated links, then the introduction of mode delay compensation does not significantly increases the total noise. From Fig. 16 it can be concluded that there is a trade-off between DSP complexity given the GD spread and an increase of the nonlinear noise.

To design the optimum FMF link, we will compare the total nonlinear noise falling at the center of the LP_{01} mode, considering the transmission of an optical super-channel with a bandwidth of 1 THz over a given FMF link to that a SMF link, for a broad range of local *DMD* values and *XT* values. The nonlinear signal field generated after 100 km was found by following the numerical method presented in Section 10.8.

Fig. 17 shows a contour plot of the normalized nonlinear noise power (in dB) generated at the center of the WDM band in the LP_{01} mode, as a function of mode coupling strength and DMD. Simulations considered the fiber characteristics in Table 1, *DMD* value sweeping was obtained by scaling the GD vector in Table 1. The nonlinear noise was normalized to the LP_{01} intra-modal nonlinear noise power obtained in the absence of coupling. In Fig. 17, two DMD managed scenarios are shown: (a) 1 segment and (b) 25 segments. Note that, the contour line highlighting the regions from Fig. 12 in Section 10.7 where the GD spread was higher than 800 ps has been overlapped. In Fig. 17, it can be seen that the nonlinear noise decreases by increasing either the *DMD* value or the *XT* value. Moreover, it can be noted that the nonlinear noise increases with the number of segments, as the contour lines move to higher *DMD* and *XT* values analogously to the enhancement observed for resonant chromatic dispersion managed systems. However, such increase is generally lower than 0.5 dB for the same (*DMD*, *XT*) value as found in [41]. For long period GD maps (Fig. 17-a), the optimum design appears to be to maximize the mode coupling, and operate at the highest possible DMD. However, for shorter period GD-managed maps (Fig. 17-b), for *XT* ranging from -40 to -30 dB/100m since the DMD tolerance increases faster with the number of segments than the nonlinear noise, system performance can be improved by increasing the number of segments and allowing for higher *DMD* values. Importantly, the optimum solution for each GD map (at the highest tolerable DMD for the highest *XT* considered) shows negligible difference in the predicted nonlinear noise.

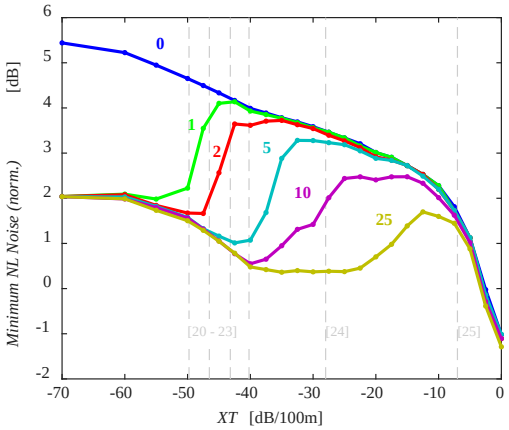

Figure 18. Minimum nonlinear noise power (normalized) as a function of the mode coupling strength, for a broad range of GD maps ranging from unmanaged to short period.

Fig. 18 shows the nonlinear performance for the highest tolerable DMD (such that GD spread < 800 ps as in Fig. 17) for a broad range of DMD maps. It can be seen that for the XT values given suppression of NL below that of uncoupled propagation, the usage of DMD compensation plays no role. Thus, it can be concluded that the usage of high *XT* fibers is preferable given that the deployment complexity associated with GD compensation is removed and fibers with relatively with *DMD* (up to 150 ps/km according to Fig. 17) can still be used.

10.11 MANAKOV APPROXIMATION VS FULLY STOCHASTIC PROPAGATION

In this section, the link conditions under which the Manakov approximation are accurately established, in terms of uncoupled DMD and linear coupling strength. The validation results in the following consider only mode delay uncompensated links as further results for DMD compensated links generated similar results. The simulations setup and the linear DSP blocks are summarized in the following.

The simulation setup is shown in Fig. 19. Over each polarization mode was transmitted an optical super-channel consisting of 3 channels spaced of 14.1 GHz carrying 14 Gbaud 16-QAM signals, giving a total bit rate of 2 Tb/s (672 Gb/s per wavelength). Together with the information

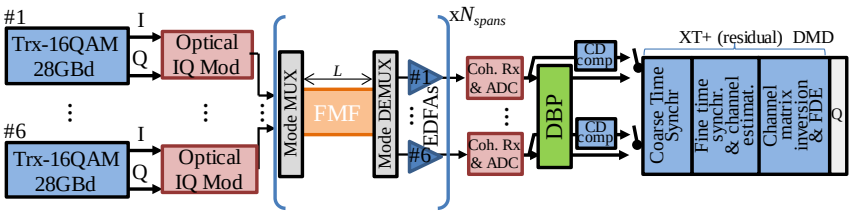

Figure 19. Block diagram for system simulations using a 6 LP modes.

data, a preamble was transmitted consisting of constant amplitude zero autocorrelation (CAZAC) sequences, used for time synchronization and channel estimation. Root raised cosine filters with a roll-off factor of 0.001 were used for pulse shaping. Simulations considered 2^{16} symbols per polarization mode, from which 2^{11} were CAZAC symbols. After homodyne detection, the baseband electrical signals were sampled at 56 GS/s, yielding 12 digital signals at 2 samples/symbol. Afterwards, the coherently received signals were compensated for chromatic dispersion in the frequency domain using the values in Table 1. In all cases, mode coupling and (residual) DMD were subsequently compensated for using data-aided channel estimation and equalization, as shown in Fig. 19. Coarse time synchronization was performed using the Schmidl & Cox autocorrelation metric. Subsequently, fine-time synchronization and channel impulse response (CIR) estimation were performed by cross-correlating with the training CAZAC sequences. The 12×12 CIR estimations were converted into the frequency domain. The MIMO frequency domain equalizer was calculated by inverting the channel matrix, and, finally, the *Q-factor* for each received signal was calculated using the mean and standard deviation of the received symbols. In the following, the *Q-factor* was averaged over the 12 polarization modes considering only the center channels.

The fiber attenuation is fully compensated using an array of 6 erbium doped fiber amplifiers [43], considering a noise figure of 3dB and negligible mode dependent gain since the aim of this paper is to assess the isolated impact of mode coupling and mode delay on the Manakov approximation. Moreover, the mode multiplexer (MUX) and de-multiplexer (DEMUX) are assumed ideal for the same reasons.

System performance simulations considered transmission over only 3 spans of 50 km such that at moderate launch signal powers (-5 to 0 dBm) performance was limited by nonlinear noise rather than by spontaneous emission noise, thus enhancing the limitations of the different

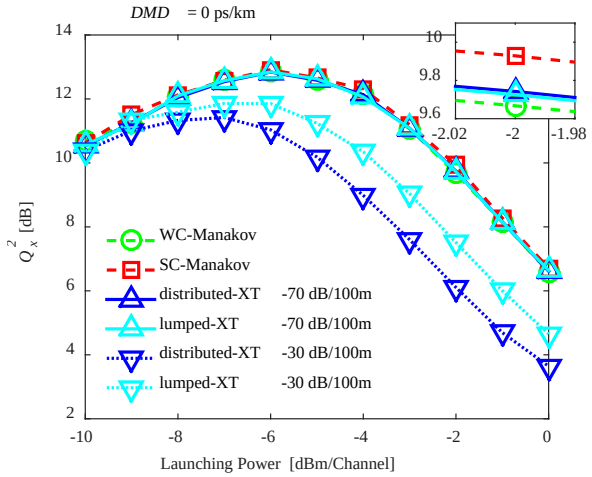

Figure 20. *Q-factor* as a function of launching signal power in the absence of DMD two different *XT* values: -70 dB/100m (WC-regime), and -30 dB/100m (intermediate coupling regime).

approximated nonlinear modelling models. The *DMD* value was varied by scaling the mode group delay values in Table 1 to allow for an objective assessment of the Manakov approximation as other fiber characteristics are kept. The *XT* value was varied from -70 to 0 dB/100m (following Section 10.8.3) covering the range of coupling values presented in the literature [20, 22, 23]. The step size was selected by bounding the local error to be lower than 10^{-5}, lower error bounds generated negligible results change.

Simulations included four different methods for the solution of (30), namely: the WC-Manakov approximation (2) [8]; the SC-Manakov (3) [7, 8] approximation; the distributed mode coupling model using the approach presented in Section 10.8.3; a lumped mode coupling model according which random unitary matrices are introduce every L_{lumped} (like in [8]), such that $XT_{[dB/100m]} + 10\log_{10}(L_{lumped}[m]/100[m]) = 0$ dB. To improve the accuracy of the SC-Manakov model, the uncoupled GD vector was scaled by the ratio of the standard deviation of the coupled GD vector obtained for $XT = -\infty$ dB/100m and the *XT* under consideration, using equation (23) in [6] derived through an analytical statistical analysis.

Fig. 20 shows the *Q-factor* as a function of launching power in the absence of DMD for two different *XT* values: -70 dB/100m (WC-regime), and -30 dB/100m (intermediate coupling regime). The figure shows that all models seem to agree for the WC-regime (-70dB/100m), but not so much for the intermediate regime (-30dB/100m). The SC-Manakov and lumped XT models differ by more than 0.5 dB from the distributed XT model in the nonlinear regime. Further insight can be obtained by varying the *XT* and *DMD* while maintaining a given launching signal power in the nonlinear regime.

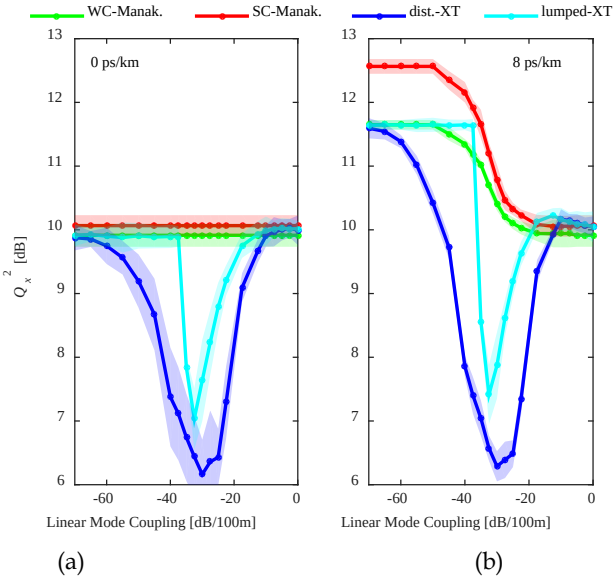

Figure 21. *Q-factor* as a function of mode coupling strength for different channel models/approximations, for -2 dBm/ch and for uncoupled DMD equal to: (a) 0 ps/km, and (b) 8 ps/km. Shadow accounts for 3-times the standard deviation given 20 repetitions.

Fig. 21 shows the *Q-factor* as a function of *XT* for different models, with 2 dBm/ch, in: (a) the absence of DMD, and (b) the presence of a low *DMD* value, 8 ps/km. First, in all cases Fig. 21-(a) and -(b), WC-Manakov and lumped XT models are in agreement with the distributed XT model for $XT < -50$dB/100m, conversely, SC-Manakov and lumped XT models are in agreement with the distributed XT model for $XT > -10$dB/100m.

However, in the intermediate coupling regime and for all three DMD cases, the WC- and SC-Manakov models as well as the lumped XT models differ by more than 0.5 dB from the distributed XT model. More importantly, it can be seen that system performance in the nonlinear regime can in fact degrade with increasing XT for low-to-intermediate values (-50 to -30 dB/100m) before it eventually approaches the SC-regime and performance improves above that of the WC-regime, as in Fig. 21-(a). Such behavior can be explained considering that for a certain range of intermediate XT values, additional pathways to FWM phase matching are created without introducing sufficiently fast random rotations of the polarization state of the field along the fiber length which would reduce the efficiency of the overall nonlinear process.

Fig. 21-(b) shows yet another scenario, within the SC-regime, performance degrades with increasing XT. In this case, the performance degradation is due to the severe reduction of the overall GD which allows for phase matching between pairs of modes which were not possible for $XT = -\infty$ dB/100m given the relative narrow bandwidth

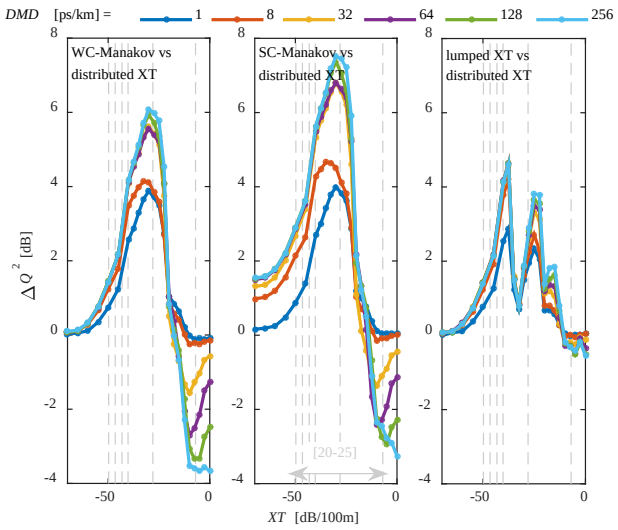

(a) (b) (c)

Figure 22. *Q-factor* error as a function of mode coupling strength, with the distributed XT model as reference, for different models: (a) WC-Manakov model, (b) SC-Manakov model, and (c) lumped XT model. Data points have been averaged over 20 repetitions.

(42 GHz) of the super-channel considered. Note that the increased penalty is relatively small given that XT reduces GD spread as well as the overall nonlinear coefficients, as explained in Section 10.8.2. Finally, this explanation is in agreement with the behavior of the SC-Manakov model given the GD vector scaling discussed earlier.

In overall, Fig. 21 shows that to some extent lumped XT model captures the behavior of the distributed model, even though overestimating performance by slightly more than 0.5 dB. Finally, Fig. 22 shows *Q-factor error* as a function of mode coupling strength, with the distributed XT model as reference. For extremely small *XT* values (< -60 dB/100m) WC-Manakov generates accurate results, however practical fibers have $XT \geq$ -50 dB/100m. For high *XT* values (> -10 dB/100m), SC-Manakov is only accurate if $DMD <$ 10 ps/km, however practical fibers have higher *DMD* in particular for more than 3-modes, besides the usage of moderate–to-high *DMD* fibers in GD-managed links. The lumped XT model is able to accurately model FMF propagation for $XT >$ -10 dB/100m even for *DMD* several times higher than 100ps/km, a practical scenario, thus a useful model. Finally, in the intermediate coupling regime (all other *XT* values) only a distributed XT model capable of introducing controllable amounts of XT with a small step-size (1-to-100m) can accurately model transmission.

10.12 CONCLUSIONS

This chapter reviewed the modelling of the linear and nonlinear impairments of few-mode fibers, namely mode group-delay spread, linear mode coupling, and intermodal nonlinear effects. Propagation over few-mode fibers is modelled deriving a few-mode split-step Fourier method composed of three steps: dispersion step, nonlinear step, and a linear mode coupling step.

The linear mode coupling step is implemented using semi-analytical solutions capable of introducing arbitrary strength coupling in a distributed manner and allowing a time efficient computation after any real-world fiber length. The model proved to be accurate against analytical predictions for the statistics of group-delays in few-mode fiber links, namely: standard deviation, probability density function, and cumulative distribution function. It proved accurate for different transmission lengths 10 m-to-10,000 km, in any coupling

regime -50 dB/100m to 0 dB/100m, without and with group-delay management.

The derived few-mode split-step Fourier method, using the linear mode coupling semi-analytical solutions, proved accurate against the analytical integration of the total nonlinear noise for optical super-channel with rectangular power spectral densities. Using the proposed model, the optimum link configurations minimizing the nonlinear penalty at practical levels of equalization complexity were obtained, namely: the coupling strength required to give suppression of nonlinear distortion below the isolated propagation without mode coupling, for different mode delay maps. Furthermore, the proposed model was used to validate the application requirements of models based on Manakov or lumped XT approximations. The Manakov approximations are proved to be accurate only for the extreme regimes not likely in practice (< -50 dB/100m, or > -10 dB/100m with DMD < 10ps/km), and the lumped XT model was found to overestimate the system performance by 0.5-to-4 dB in the intermediate coupling regime.

Finally, the reviewed modelling methods are essential tools for the modelling and development of future high-capacity multimode fiber systems, in particular for the intermediate coupling regime.

10.13 ACKNOWLEDGEMENTS

This work has been partially supported by the EU (654809-HSPACE and 659950-INVENTION), and by EPSRC (EP/L000091/1-PEACE).

10.14 RESEARCH DATA

The Matlab scripts, source C-code, mex compiled C-code, and figure data points are available at https://doi.org/10.17036/researchdata.aston.ac.uk.00000338.

10.15 REFERENCES

1. Richardson, D.J., J.M. Fini, and L.E. Nelson, *Space-division multiplexing in optical fibres.* Nature Photonics, 2013. **7**: p. 354.
2. Li, G., et al., *Space-division multiplexing: the next frontier in optical*

communication. Advances in Optics and Photonics, 2014. **6**(4): p. 413-487.
3. Marcuse, D., A. Telephone, and T. Company, *Theory of Dielectric Optical Waveguides*. 1991: Academic Press.
4. Ho, K.-P. and J.M. Kahn, *Linear Propagation Effects in Mode-Division Multiplexing Systems.* Journal of Lightwave Technology, 2014. **32**(4): p. 614-628.
5. Antonelli, C., A. Mecozzi, and M. Shtaif, *The delay spread in fibers for SDM transmission: dependence on fiber parameters and perturbations.* Opt Express, 2015. **23**(3): p. 2196-202.
6. Ferreira, F.M., et al., *Semi-Analytical Modelling of Linear Mode Coupling in Few-Mode Fibers.* Journal of Lightwave Technology, 2017. **35**(18): p. 4011-4022.
7. Mecozzi, A., C. Antonelli, and M. Shtaif, *Nonlinear propagation in multi-mode fibers in the strong coupling regime.* Optics Express, 2012. **20**(11): p. 11673-11678.
8. Mumtaz, S., R.-J. Essiambre, and G.P. Agrawal, *Nonlinear Propagation in Multimode and Multicore Fibers: Generalization of the Manakov Equations.* Journal of Lightwave Technology, 2013. **31**(3): p. 398-406.
9. Rademacher, G. and K. Petermann, *Nonlinear Gaussian Noise Model for Multimode Fibers With Space-Division Multiplexing.* Journal of Lightwave Technology, 2016. **34**(9): p. 2280-2287.
10. Ferreira, F.M., et al. *Advantages of strong mode coupling for suppression of nonlinear distortion in few-mode fibers*. in *2016 Optical Fiber Communications Conference and Exhibition (OFC)*. 2016.
11. Ho, K.-P. and J.M. Kahn, *Statistics of Group Delays in Multimode Fiber With Strong Mode Coupling.* Journal of Lightwave Technology, 2011. **29**(21): p. 3119-3128.
12. Keang-Po, H. and J.M. Kahn, *Delay-Spread Distribution for Multimode Fiber With Strong Mode Coupling*. IEEE Photonics Technology Letters, 2012. **24**(21): p. 1906-1909.
13. Antonelli, C., et al., *Stokes-space analysis of modal dispersion in fibers with multiple mode transmission.* Optics Express, 2012. **20**(11): p. 11718-11733.
14. Mecozzi, A., C. Antonelli, and M. Shtaif, *Intensity impulse response of SDM links.* Opt Express, 2015. **23**(5): p. 5738-43.
15. Ye, F., S. Warm, and K. Petermann. *Differential Mode Delay Management in Spliced Multimode Fiber Transmission Systems*. in *Optical Fiber Communication Conference/National Fiber Optic Engineers Conference 2013*. 2013. Anaheim, California: Optical Society of America.
16. Juarez, A.A., et al., *Modeling of Mode Coupling in Multimode Fibers*

With Respect to Bandwidth and Loss. Journal of Lightwave Technology, 2014. **32**(8): p. 1549-1558.
17. Ferreira, F., et al., *Nonlinear Semi-Analytical Model for Simulation of Few-Mode Fiber Transmission.* IEEE Photonics Technology Letters, 2012. **24**(4): p. 240-242.
18. Ferreira, F., P. Monteiro, and H. Silva. *Semi-analytical model for linear modal coupling in few-mode fiber transmission*. in *2012 14th International Conference on Transparent Optical Networks (ICTON)*. 2012. IEEE.
19. Ferreira, F., et al., *Reach Improvement of Mode Division Multiplexed Systems Using Fiber Splices.* IEEE Photonics Technology Letters, 2013. **25**(12): p. 1091-1094.
20. Gruner-Nielsen, L., et al., *Few Mode Transmission Fiber With Low DGD, Low Mode Coupling, and Low Loss.* Journal of Lightwave Technology, 2012. **30**(23): p. 3693-3698.
21. Mori, T., et al. *Low DMD four LP mode transmission fiber for wide-band WDM-MIMO system*. in *2013 Optical Fiber Communication Conference and Exposition and the National Fiber Optic Engineers Conference (OFC/NFOEC)*. 2013.
22. Ryf, R., et al. *Space-Division Multiplexed Transmission over 4200 km 3-Core Microstructured Fiber*. in *National Fiber Optic Engineers Conference*. 2012. Los Angeles, California: Optical Society of America.
23. Fontaine, N.K., et al. *Experimental investigation of crosstalk accumulation in a ring-core fiber*. in *2013 IEEE Photonics Society Summer Topical Meeting Series*. 2013.
24. Antonelli, C., et al., *Random coupling between groups of degenerate fiber modes in mode multiplexed transmission.* Opt Express, 2013. **21**(8): p. 9484-90.
25. Agrawal, G., *Chapter 2 - Pulse Propagation in Fibers*, in *Nonlinear Fiber Optics (Fifth Edition)*. 2013, Academic Press: Boston. p. 27-56.
26. Ferreira, F., S. Sygletos, and A. Ellis. *Impact of linear mode coupling on the group delay spread in few-mode fibers*. in *2015 Optical Fiber Communications Conference and Exhibition (OFC)*. 2015.
27. Ferreira, F.M., et al. *Few-mode fibre group-delays with intermediate coupling*. in *2015 European Conference on Optical Communication (ECOC)*. 2015.
28. Suibhne, N.M., et al. *Experimental verification of four wave mixing efficiency characteristics in a few mode fibre*. in *39th European Conference and Exhibition on Optical Communication (ECOC 2013)*. 2013.
29. Antonelli, C., A. Mecozzi, and M. Shtaif. *Scaling of inter-channel nonlinear interference noise and capacity with the number of strongly*

coupled modes in SDM systems. in *2016 Optical Fiber Communications Conference and Exhibition (OFC)*. 2016.

30. Ferreira, F., et al. *Nonlinear Transmission Performance in Delay-Managed Few-Mode Fiber Links with Intermediate Coupling*. in *Optical Fiber Communication Conference*. 2017. Los Angeles, California: Optical Society of America.
31. Palmieri, L. and A. Galtarossa, *Coupling Effects Among Degenerate Modes in Multimode Optical Fibers.* IEEE Photonics Journal, 2014. **6**(6): p. 1-8.
32. H., W., et al., *Numerical Recipes 3rd Edition: The Art of Scientific Computing*, ed. N.Y.C. University. 2007.
33. Mathews, J. and K. Fink, *Numerical Methods Using Matlab*, ed. P. Hall. 1999.
34. Ferreira, F.M., D. Fonseca, and H.J.A. da Silva, *Design of Few-Mode Fibers With M-modes and Low Differential Mode Delay.* Journal of Lightwave Technology, 2014. **32**(3): p. 353-360.
35. Noda, J., K. Okamoto, and Y. Sasaki, *Polarization-maintaining fibers and their applications.* Journal of Lightwave Technology, 1986. **4**(8): p. 1071-1089.
36. Fan, S. and J.M. Kahn, *Principal modes in multimode waveguides.* Optics Letters, 2005. **30**(2): p. 135-137.
37. Arik, S.O., K.-P. Ho, and J.M. Kahn, *Delay Spread Reduction in Mode-Division Multiplexing: Mode Coupling Versus Delay Compensation.* Journal of Lightwave Technology, 2015. **33**(21): p. 4504-4512.
38. Randel, S., et al. *Mode-Multiplexed 6×20-GBd QPSK Transmission over 1200-km DGD-Compensated Few-Mode Fiber*. in *Optical Fiber Communication Conference*. 2012. Los Angeles, California: Optical Society of America.
39. Sinkin, O.V., et al., *Optimization of the split-step fourier method in modeling optical-fiber communications systems.* Journal of Lightwave Technology, 2003. **21**(1): p. 61-68.
40. Ellis, A.D., et al., *Expressions for the nonlinear transmission performance of multi-mode optical fiber.* Opt Express, 2013. **21**(19): p. 22834-46.
41. Rademacher, G., S. Warm, and K. Petermann, *Analytical Description of Cross-Modal Nonlinear Interaction in Mode Multiplexed Multimode Fibers.* IEEE Photonics Technology Letters, 2012. **24**(21): p. 1929-1932.
42. Sinkin, O.V., et al. *Impact of broadband four-wave mixing on system characterization*. in *2013 Optical Fiber Communication Conference and Exposition and the National Fiber Optic Engineers Conference (OFC/NFOEC)*. 2013.
43. Rademacher, G., et al., *Long-Haul Transmission over Few-Mode*

Fibers with Space-Division Multiplexing. Journal of Lightwave Technology, 2017. **PP**(99): p. 1-1.